IMAGE RECONSTRUCTION IN DENTAL TOMOSYNTHESIS WITH STATIONARY DETECTOR

by

Yunus Burak Sur

B.S., in Electronics Engineering, Sabancı University, 2010

Submitted to the Institute of Biomedical Engineering

in partial fulfillment of the requirements

for the degree of

Master of Science

in

Biomedical Engineering

Boğaziçi University

2019

IMAGE RECONSTRUCTION IN DENTAL TOMOSYNTHESIS WITH STATIONARY DETECTOR

APPROVED BY:

Prof. Dr. Cengizhan Öztürk ....
(Thesis Advisor)

Assoc. Prof. Dr. Albert Güveniş ....

Assist. Prof. Dr. Murat Tümer ....

DATE OF APPROVAL: 6 September 2019

ACKNOWLEDGMENTS

ACADEMIC ETHICS AND INTEGRITY STATEMENT

I, Yunus Burak Sur, hereby certify that I am aware of the Academic Ethics and Integrity Policy issued by the Council of Higher Education (YÖK) and I fully acknowledge all the consequences due to its violation by plagiarism or any other way.

Name :

Signature:

_____

_____

Date:

_____

ABSTRACT

IMAGE RECONSTRUCTION IN DENTAL TOMOSYNTHESIS WITH STATIONARY DETECTOR

Tomosynthesis is an imaging modality for analyzing anatomical structures. X-ray images from different angles are used for reconstruction in tomosynthesis. In contrast to computed tomography, X-ray tube moves around a restricted pathway for acquisition. Therefore, number of projections are used for reconstruction are less than computed tomography.

In this thesis, feasibility of tomosynthesis was explored for a stationary detector system, where x-ray tube had a limited circular movement around isocenter. Algorithms are both used for simulation and physical phantom. X-ray simulation is created based on x-ray attenuation and ray tracing. Physical phantom is produced for acquisition of images with x-ray machine. Observations were made for different conditions in image creation. Effects of the range of circular movement and step size were analyzed. Also, influence of angles between selected plane and axes in image formation were studied. Additionally, effect of selected plane to isocenter distance was experimented. Lastly, artifact and blur removal was applied to achieve better structure identification.

Analysis of reconstructed images showed that tomosynthesis could improve the identification of structures. Wider acquisition arcs, artifact and blur removal were the most important factors in getting better images. Planes other than the focused plane caused artifacts and blur in reconstructed image. Therefore, planes with high contrast objects were subtracted from reconstructed plane to improve the visibility of the objects. Histogram analysis also showed the suppression of higher contrast pixels in the reconstructed image.

Keywords: Medical imaging, X-ray imaging, Tomosynthesis, Limited angle imaging, Stationary detector.

ÖZET

SABİT DETEKTÖRLÜ DENTAL TOMOSENTEZDE GÖRÜNTÜNÜN YENİDEN OLUŞTURULMASI

Tomosentez anatomik yapıları analiz etmek için kullanılan bir görüntüleme yöntemidir. Tomosentezde, farklı açılardan çekilen X-ışını görüntüleri, görüntünün yeniden oluşturulması için kullanılır. Bilgisayarlı kesityazarın aksine, X-ışını tüpü çekim için kısıtlı bir yol üzerinde hareket eder. Bu sebeple, yeniden oluşum için kullanılan izdüşümlerinin sayısı bilgisayarlı kesityazardan daha azdır.

Bu tezde, x-ışını tüpünün kısıtlı bir çember üzerinde eşmerkez etrafında hareket edebildiği, sabit detektörlü tomosentez sisteminin uygulanabilirliği araştırıldı. Algoritma hem benzetim hem de fiziksel fantom için kullanıldı. X-ışını soğrulması ve ışın izlemeye dayanılarak x-ışını benzetimi oluşturuldu. X-ışını makinesiyle görüntü almak için fiziksel fantom üretildi. Görüntü oluşumu farklı koşullar altında gözlemlendi. Dairesel hareketin aralığının ve adım boyutunun etkileri incelendi. Ayrıca, seçilen düzlem ile eksenler arasındaki açının görüntü oluşumuna etkisi araştırıldı. Ek olarak, seçilen düzlem ile eşmerkez arasındaki mesafenin etkisi denendi. Son olarak, yapıların dahi iyi tanımlanması için yapay oluşumların ve bulanıklığın giderimi işlemi uygulandı.

Yeniden oluşturulan görüntülerin analizi gösterdi ki, tomosentez, yapıların daha iyi tanımlanmasını sağlayabilir. İyi görüntü oluşumunda daha geniş yakalama yayı, yapay oluşumların ve bulanıklığın giderimi en önemli etkenlerdir. Odak düzlemi dışındaki düzlemler, yeniden oluşturulan görüntülerde yapay oluşumlar ve bulanıklığa sebep olmaktadır. Bu nedenle, objelerin görünebilirliğini iyileştirmek için yüksek kontrastlı objelerin bulunduğu düzlemler, yeniden oluşturulan düzlemden çıkarılmaktadır. Histogram analizi de görüntüdeki yüksek kontrastlı piksellerin baskılanmasını göstermiştir.

Anahtar Sözcükler: Tıbbi görüntüleme, X-ışını görüntüleme, Tomosentez, Kısıtlı açıda görüntüleme, Sabit dedektör.

TABLE OF CONTENTS

LIST OF FIGURES

LIST OF TABLES

LIST OF SYMBOLS

K_α	Characteristic x-rays
K_β	Characteristic x-rays
N_0	Total number of photons
N_{in}	Initial photon number
μ	Material specific attenuation coefficient
t	Distance travelled
τ	Photoelectric absorption
σ	Compton scattering
I_{in}	Intensity value of the corresponding radiation energy
I_d	Intensity value of x-ray at the selected plane
$\mu(x, y, z, E)$	Linear attenuation in each section
E	Energy
μ_0	Uniform linear attenuation coefficient
ω	Angle between x-ray tube and vertical axis
x_i	Object point's projection at image plane
x_i'	Object point's projection at image plane for different angle ω
b	Isocenter to x-ray source distance
D_n	Isocenter to image plane distance
x	Object point
z	Object point
x_d	Distance between source and detector in x axis
y_d	Distance between source and detector in y axis
z_d	Distance between source and detector in z axis
S_x	Source position in x axis
S_y	Source position in y axis
S_z	Source position in z axis
D_x	Detector position in x axis

D_y	Detector position in y axis
D_z	Detector position in z axis
t_l	Variable to set distance between source and current point line
ΔS	Pixel surface
$\Delta \Omega$	Solid angle
K	Pixel center
n_s	Normal vector to the detector surface
u_s	Unit vector for source to pixel center K
θ_s	Angle between n_s and u_s
r_s	Distance Source position to pixel center
N_s	Photon number that reaches to the detector
N_s^0	Photon number with energy E for solid angle $\Delta \Omega$ at source
μ_{mt}	Linear attenuation coefficient for object mt
x_{mt}	Distance travelled in object mt
M	Isocenter point
MG	Points denotes plane at isocenter
$M_i G_i$	Points denotes image's position at image intensifier
$M_{\hat{h}} G_{\hat{h}}$	Points denotes image's projection at horizontal plane
d	Source to image intensifier distance
i	Column position at intensifier plane
j^*	Row position at intensifier plane
l	Plane distance to isocenter
QT	Plane points at distance l
$Q_{\hat{i}} T_{\hat{i}}$	Projection of QT at image intensifier
$Q_{\hat{r}} T_{\hat{r}}$	Reconstructed image of QT
$\hat{\alpha}$	Angle between selected plane and vertical in x axis
$\hat{\beta}$	Angle between selected plane and vertical in y axis
QU	Points of plane when it has $\hat{\alpha}$ with vertical
$\hat{q}$	Distance between points $Q_{\hat{r}}$ and $M_{\hat{r}}$
$\hat{h}$	Column position at horizontal plane

$\hat{r}$	Column position at image formation plane
k	Projection of row j^*
Δh	Shifting applied on image plane
l_k	Height between selected plane intersection with central axis and point on selected plane
$\hat{u}$	Magnification for image row when plane is not at isocenter
r_o	Final row position
m_{st}	Magnification factor for stationary detector system
s_{st}	Shift distance for stationary detector system
I_{SP}	Tomosythesized image of selected plane
I_{NP}	Tomosythesized image of distortion inducing plane
$\hat{h}_{NP}$	Column position of distortion inducing plane's projection at horizontal plane
$\hat{r}_{NP}$	Column position of distortion inducing plane's projection at image formation plane
$\hat{m}_{NP}$	Magnification used for distortion inducing plane tomosynthesis
$\delta\hat{h}_{NP}$	Shift used for distortion inducing plane tomosynthesis
$\hat{r}_{N,S}$	New column position for mask image
$\delta\hat{h}_{SP}$	Shift used for selected plane tomosynthesis
$\hat{m}_{SP}$	Magnification used for selected plane tomosynthesis
$\acute{x}$	Image signal
$\acute{y}$	Image signal
$\tau_{\acute{x}}$	Mean intesity value of image signal $\acute{x}$
$\tau_{\acute{y}}$	Mean intesity value of image signal $\acute{y}$
$\sigma_{\acute{x}}$	Standard deviation of image signal $\acute{x}$
$\sigma_{\acute{y}}$	Standard deviation of image signal $\acute{y}$
C_1	Constant
C_2	Constant
$\acute{X}$	Reference image for comparison
$\acute{Y}$	Distorted image for comparison

W^T	Total number of local windows
wn	Current window number
$\acute{x}_{wn}$	Reference image information at window wn
$\acute{y}_{wn}$	Distorted image information at window wn

LIST OF ABBREVIATIONS

CT	Computed Tomography
SAA	Shift and Add Algorithm
MITS	Matrix Inversion Tomosynthesis
FBP	Filtered Backprojection
TACT	Tuned Aperture Computed Tomography
ART	Algebraic Reconstruction Technique
SIRT	Simultaneous Iterative Reconstruction Technique
MPA	Multiple Projection Algorithm
SSIM	Structure Similarity Index
MSSIM	Mean Structure Similarity Index
SID	Source to detector Distance
SOD	Source to patient Distance

1. INTRODUCTION

Importance of the imaging modalities are increasing in diagnostic radiology. Tomosynthesis is one of the techniques that used for imaging. Digital tomosynthesis is x-ray based imaging technique for structure analysis. Images are acquired as a set of images at different position of the tube. In medicine, tomosynthesis helps to determine anatomical structures more accurately with low radiation exposure [1].

In standard tomography techniques, image is acquired continuously. Study on tomography, showed that it is possible to reconstruct planes form the discrete series of image projections. Later, development of the design enabled the full three dimensional image dataset acquisition. First circular based imaging technique was accomplished by Grant [2].

Tomosynthesis is also used in various areas of the medicine such as angiographic imaging, chest tomosynthesis, breast imaging, orthopedic and dental tomosynthesis.

Aim of this thesis is to accomplish detailed images of the structure by using the tomosynthesis methods. With the help of the images, problems can be diagnosed more easily with better distinction between anatomical structures. For the purpose of this thesis; a reconstruction algorithm is implemented for limited angle x-ray projections created by a stationary detector system. Then effects of the positions of the selected planes on the reconstructed image are investigated. Also, blur and artifacts on the reconstructed image are minimized to improve the image quality.

The thesis is divided into 5 chapters. After this introduction chapter, information on x-rays and tomosynthesis are given in Chapter 2. X-ray simulation, tomosynthesis, distortion removal, and image quality assessment methods used in this thesis are explained in Chapter 3. Results and relevant discussion are given in Chapter 4. Lastly, findings and possible future works are briefly mentioned in Chapter 5.

2.   BACKGROUND

2.1   X-rays

2.1.1   How x-rays found

Wilhelm Röntgen noticed x-rays during his work on cathode tubes. In these studies, he was focusing electric current on very low gas pressure [3]. Fluorescent screen included in these works which glowed as result of tube's light emission. During experiments, tube was placed into carton box that prevented light emission but screen continued to be fluorescent. As result he discovered another type of radiation which he called x-rays [4]. His continued experiments on subject showed that objects with different size on the route of the rays effected result on the photographic plate. Later, he captured the image of his wife's hand. This picture was the first Röntgen image that revealed her bones, ring and shadow of her soft tissue [3].

2.1.2   Interaction of particles and x-ray photon

2.1.2.1   Characteristic x-ray.   X-ray photons emerge after interaction in atoms. Atom is a structure that consists of nucleus and electrons settled on orbits. Nucleus includes protons and neutron which determines atomic mass. Charge of an atom depends on the difference between number of protons and electrons. Every electron has different energy level when it is in a particular shell. Additionally, highest energy level for each shell varies depending on the shell's position from nucleus, for example distance between K shell and the nucleus is shorter than the L shell thus K shell has higher binding energy level. An electron can change its shell or leave its atom according to energy emerged through atom quantum interactions. When atom shell has lower energy level than incident electron, shell will eject its electron. This will cause an ionized atom with an electron gap in the shell thus an electron moves to inner shell

from the outer shell to balance the unequal level of the binding energy of the shells; x-ray photon emerges as result of this electron transport. This is called characteristic x-ray. Energy of this photon depends on the type of atom. For instance, interaction in tungsten element causes 59.3 keV energy difference between K shell and L shell. Therefore, this difference creates an x-ray radiation emission with equivalent energy. Similar interaction between different shells exists but energy level of photon is not enough to contribute image formation, if K shell is not targeted [5].
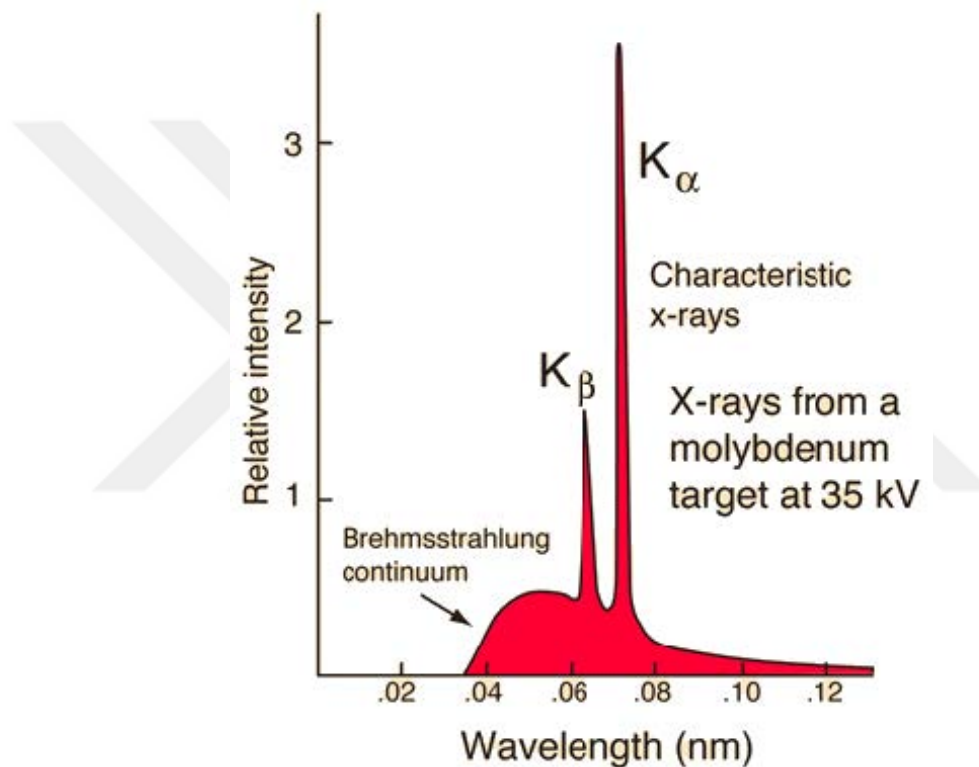
Figure 2.1 Continuous and characteristic x-rays [6].

2.1.2.2 Bremsstrahlung. Another type of emission coexists with characteristic X-ray radiation. Continuous radiation emerges when electron deaccelerated while heading to metal target. Since electrons are braked due to nucleus's electrical field which yields to the emission of radiation and this phenomenon called Bremsstrahlung which means braking radiation in German. As result of deceleration, energy is transformed into x-ray photon. Intensity and frequency of radiation is linked energy of charged particle. Higher levels of energy increases intensity and frequency distribution of the radiation [6],[7].
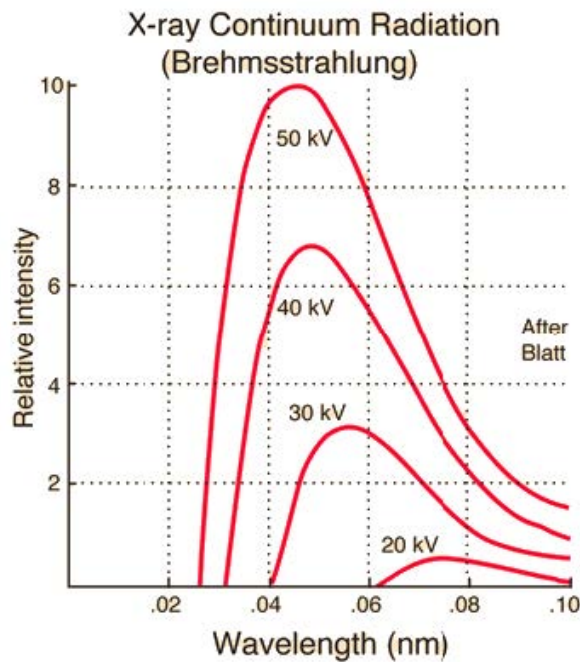
Figure 2.2 Bremsstrahlung energy radiation spectrum [6].
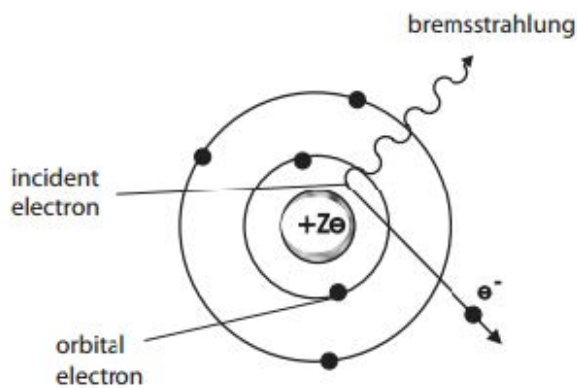
Figure 2.3 Braking electron and X-ray photon emission [7].

2.1.2.3   X-ray photons interaction with matter.   Interaction of emitted x-ray photon with tissue has four different types. First scenario is absorption of photon. When photon approaches to the nucleus atom, it will cause movement in the orbital electron in same direction. This interaction called photo electrical absorption. Secondary interaction is called Compton scattering. It occurs if x-ray photon gives its energy to electron partially. In this case photon will lose some of its energy and it

will be deflected from entrance route. Another one is pair production. It takes place
if the energy of the photon is higher than the 1.02 MeV. In this situation an electron
and positron is produced from the photon. Electron and positron have same mass but
different charges. After that positron will interact with different electron and this will
cause an emergence of two new photon with energy level at 511 keV [4].
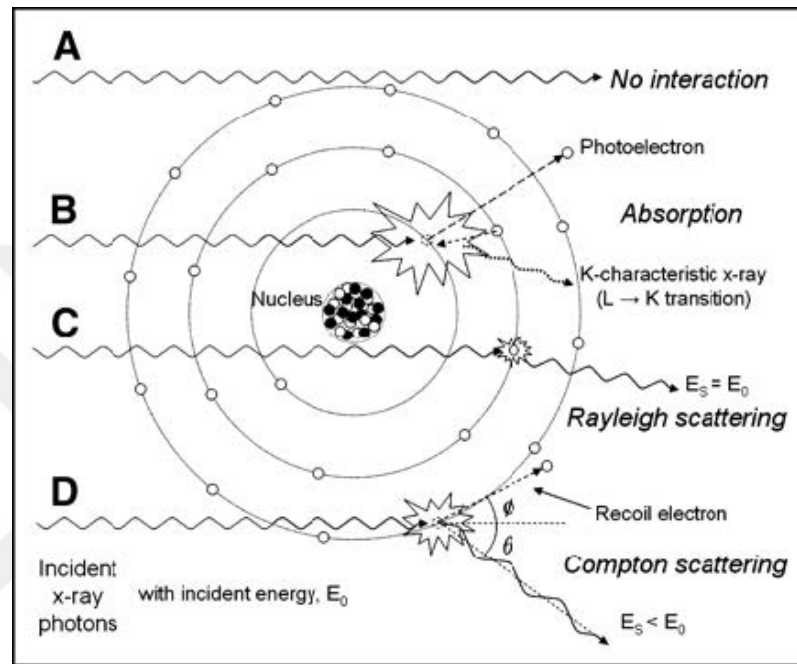
Figure 2.4 X-ray photon interaction with matter [8].

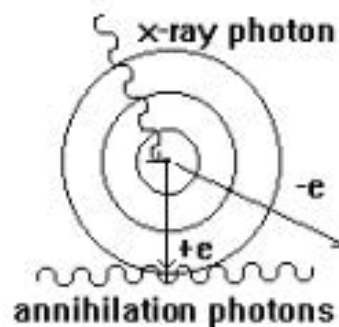**Figure 2.5** Photon production through pair production [9].

Last interaction type is Rayleigh scattering. It happens when X-ray photon
do not loss its energy due to scattering. Orbital electron's energy increases when it
affected by x-ray photon. Electron do not leave its shell but it emits x-ray photon as
result of temporary energy change. This emitted X-ray is deflected from its route with
a small angle [8].

2.1.2.4   Interaction of x-ray with tissue.   When x-ray beam passes through tissue, it loses some of its energy according to thickness and type of the material. This phenomenon is called attenuation of the ray. Dhawan [5] expressed the relation between number of photons, image intensity, thickness and attenuation coefficient with the equations below.

$$N_0 = N_{in} \cdot e^{-\mu \cdot t} \tag{2.1}$$

$$I_d(x, y) = \int I_{in}(x, y, E) \cdot e^{\int \mu(x,y,z,E) \cdot dx} d(E) \tag{2.2}$$

$$I_d(x, y) = I_{in}(x, y) \cdot e^{-\int \mu_0 \cdot t} \tag{2.3}$$

N_0 shows the total number of photon in the x-ray beam after attenuation. N_{in} is the initial photon number before penetration of x-ray to the body. μ represents the material specific attenuation coefficient and t is the distance travelled by x-ray beam through material. Intensity equation for the image can be acquired by continuous tracing of photons. Similar to photon number calculations, equations for intensity of image are given at above. N_{in} is the intensity value of the corresponding radiation energy. Id represents the intensity value of the x-ray at the selected plane: $\mu(x, y, z, E)$ is the linear attenuation and it depends on particular section of the material. When material is homogenous, μ will be constant for selected object. Assuming monochromatic x-ray radiation and constant attenuation, equation 2.3 will be acquired [5].
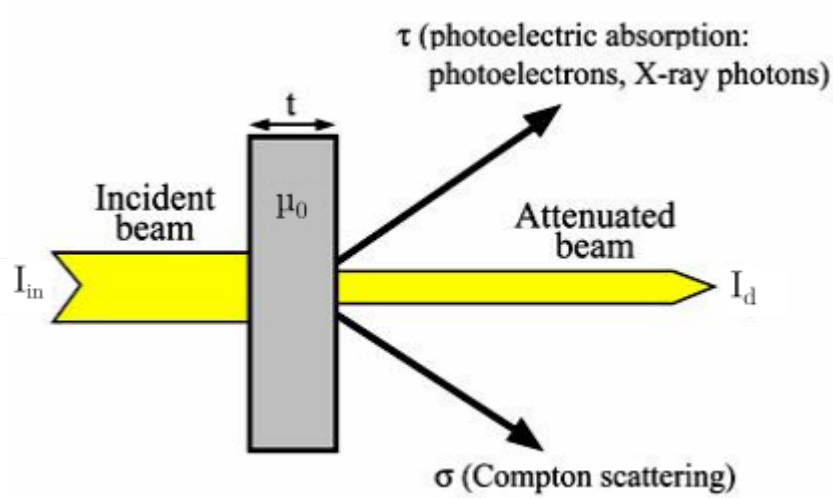
Figure 2.6 Passage of beam through matter. Adapted from [10].

2.2 Tomosynthesis

Tomographic imaging is important technique for diagnostic radiology. It helps to acquire three dimensional images of anatomic structures. In geometric tomography, x-ray tube passes through arc shaped route. Patient is exposed to photons during this movement. Image is created by the cassette on the opposite side of tube. Blurring in x-ray shadows of the structures out of focal plane creates tomographic effect. Shadows of the structures in the focal plane will be parallel to each other. Therefore, contrasts of the focal plane objects will overlap each other. But contrasts of off-plane objects will be distributed over the receptor. This distribution of objects will cause image to be blurred out [11]. Tomographic imaging is preferred mainly for three reasons. Firstly, tomography allows depth localization. Another one is the discernibility of the objects is more than conventional radiography, because imaging method facilitates the removal of visual clutter due to overlapping structures. Lastly, tomographic imaging restricts the overall dynamic range to a single slice which increases contrast of local structures [2].

Digital tomosynthesis is similar to the geometric tomography. In tomosynthesis, each image is created at different tube angle. Image acquisition through tomosynthesis is shown in Figure 2.8. Four different images are constructed from four different angles
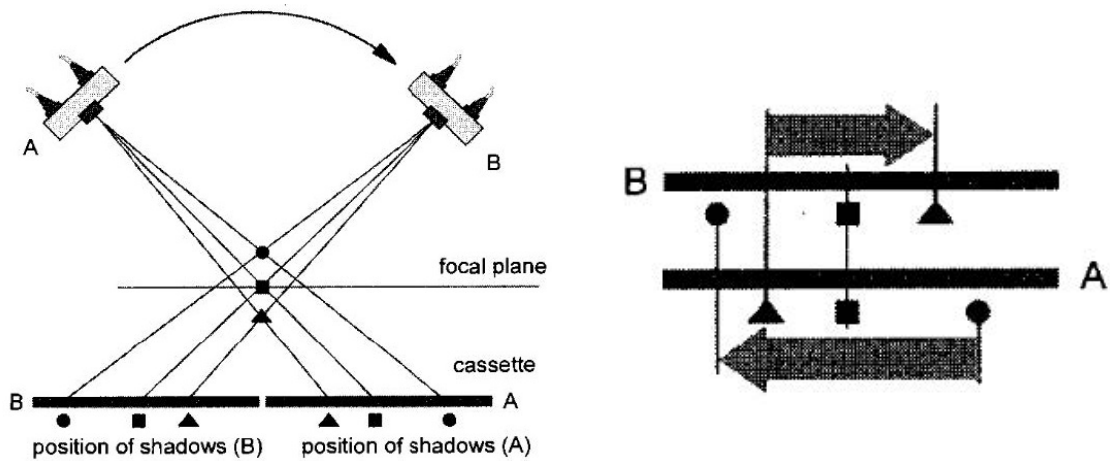
Figure 2.7 Geometric tomography system [11].

in each plane. Then these images are shifted and added to create tomographic images. Important feature of tomosynthesis is the sufficiency of same single set of images for different planes.

As shown in Figure 2.8, shifting distances determines the image composition in different planes. For instance, when image is constructed with respect to first focal plane, shift distance shown in figure is used. Object at the focal plane is overlapped while constructing image. After creation of image, it can be seen that acquired image is same with geometric imaging [11].
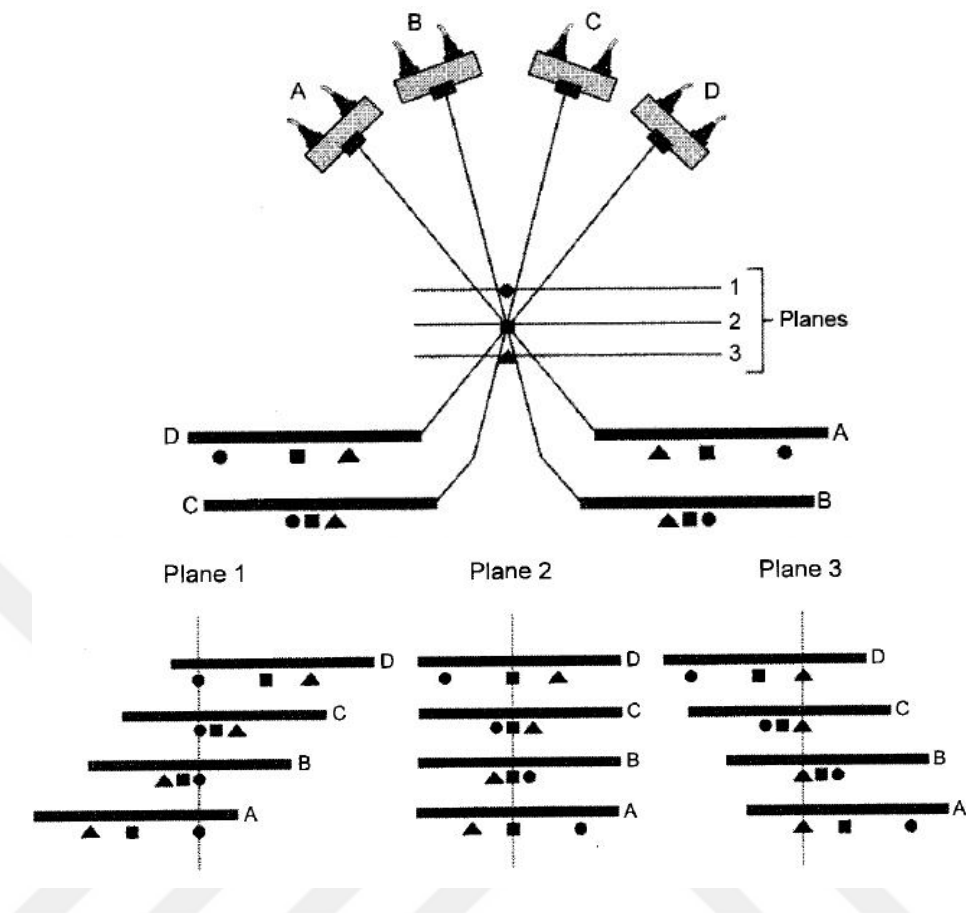
Figure 2.8 Imaging method in tomosynthesis [11].

2.2.1 Types of motion

There exist three main types of motion for tomosynthesis systems. First one is the parallel motion of tube and detector plane. In parallel motion, x-ray tube moves in a plane that is parallel to detector plane. This type of method is applied at abdominal and chest imaging for tomosynthesis. Another configuration is full isocentric motion. In this design, x-ray source and detector is attached to each other. They move on an arc with respect to each other. Center of the tube is aligned with the center of detector during motion. This method is applied in cone beam CT and also it is used for tomosynthesis research with C-arm imagers. Last configuration is partial isocentric motion. In this method, detector is stationary during scan and only tube travels through a circular path. Breast tomosynthesis images are acquired by this design. Breast is compressed between detector plane and compression plate. When reconstruction methods of these

three design are compared, parallel path tomosynthesis has the easiest algorithm for image reconstruction. Reconstruction allows stability of the magnification ratio during each position. Full isocentric motion gives best results but complexity of the algorithms is higher than other. Partial isocentric configuration causes non-uniform magnification during tube motion. For this reason distortion in object need to be processed by back projection [12] .
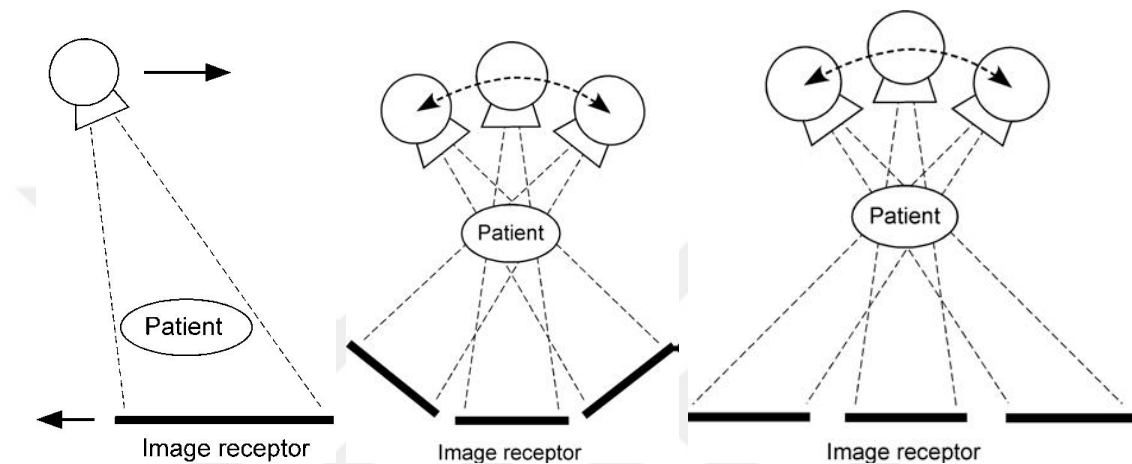

Figure 2.9 Parallel path, isocentric and partial isocentric motion [2].

2.3   Reconstruction methods for tomosynthesis

Shift and Add Algorithm (SAA) is most basic reconstruction technique used for parallel path configuration. In this algorithm, each image is taken at different position of the tube. As seen in Figure 2.8, when the objects are placed at different distances from the detector, their displacement will be changed with respect tube position, and objects will have different position in each projection. Positions of the structure depends on the relative height of the structures. In this method, x-ray tube and detector follow a parallel path. Therefore, magnification of structures only change with the height above detector. Tube and detector positions does not affect the magnification of the objects. Acquired object images in same plane will be in the same line focused. But other structures in different focal plane will appear as blurred out. Although SAA algorithm is simple, it is insufficient to create high detailed images due to blur effect caused by out of plane structures. For this reason, it is mostly used

with the de-blurring methods such as filtered back projection (FBP), matrix inversion tomosynthesis (MITS) etc. [2].

Another reconstruction method that uses isocentric property is mostly in breast tomosynthesis. In this design, detector moves in a plane or its stationary but x-ray tube follow a circle path during image acquisition. Due to stationary detector, size of the structures changes with tube angle.
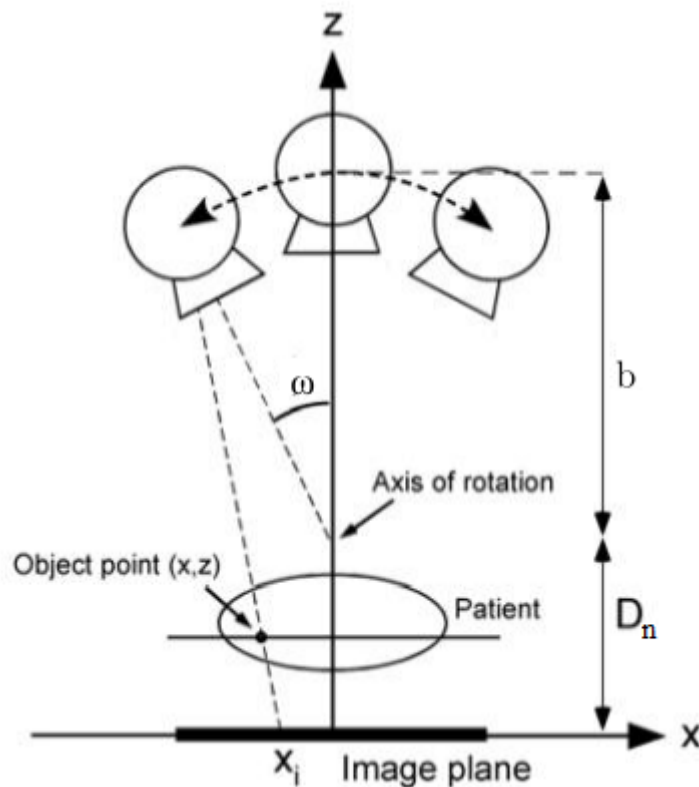
Figure 2.10 Partial isocentric motion. Adapted from [2].

$$x_i(w, x, z) = \frac{z \cdot (b \cdot \sin \omega + x)}{b \cdot \cos \omega + D_n - z} \tag{2.4}$$

As shown in Figure 2.10, specific point on the patient is projected to the image plane with a given x_i. In contrast to isocentric configuration, tube angle stays same during acquisition. This leads to the equation below.

$$x_i'(w, x, z) = x + \frac{z \cdot (b \cdot \tan \omega + x)}{b + D_n - z} \tag{2.5}$$

Both of these equations can help to transform images in isocentric geometry to parallel path geometry. Later data can be shifted and added to acquire focal planes with different heights [2].

Additional two methods for image reconstruction is iterative algorithms and Tuned Aperture Computed Tomography (TACT). Iterative techniques allow the three dimensional object visualization from the two dimensional projections. Mainly three types of iterative process exist. These are algebraic reconstruction technique (ART), simultaneous iterative reconstruction technique (SIRT) and iterative least squares technique (ILST). TACT uses fiducial markers to determine exact imaging geometry. These markers helps to find the orientation of the projection images for SAA tomosynthesis method [2].

Multiple Projection method is applied during this thesis. Therefore, detailed information in this technique will be explained in Section 3.3.

3. METHODS

3.1   X-ray simulation

First step of thesis is implementation of x-ray image creation. Then, images created by this algorithm are used for testing tomosynthesis algorithm. For this purpose, basic x-ray simulation created based on ray propagation.

Firstly, ray exits from point source and travel through a line until it hits the destination at detector. The line equation gives the x, y, z coordinates of the points in a line, which can be used for creating data points. S_x, S_y, S_z represents the location of starting point for line which is source of the x-ray. Distance between source and detector is shown by x_d, y_d, z_d. Lastly, variable t_l determines the distance between source and current point line. Considering [13]:

$$
\begin{aligned}
x &= S_x + x_d \cdot t_l \\
y &= S_y + y_d \cdot t_l \\
z &= S_z + z_d \cdot t_l
\end{aligned}
\tag{3.1}
$$

$$
\begin{aligned}
x_d &= D_x - S_x \\
y_d &= D_y - S_y \\
z_d &= D_z - S_z
\end{aligned}
\tag{3.2}
$$

During simulation, increment in t_l is limited to $1/(2 \cdot z_d)$. For example, if distance between source and detector in z axis is 8 units then t_l will rise by 0.0625 (Figure 3.1). Effect of greater increment value is shown in simulation phantom Section 4.1.1.

After all data points is acquired through line, they are stored for finding intersection between objects and x-ray. Coordinates of objects' points are stored in a matrix with corresponding attenuation values. Rays data points compared with the objects coordinates. If a ray passes through an object, its energy will decrease through line until next data point. This calculation will continue unless photon reaches the detector. Attenuation distance is fixed since data points are increasing with constant rate. When photon reaches to detector, attenuated value is written to the corresponding image location. As seen in Figure 3.2, photon number reached to the detector is related with the solid angle $\Delta\Omega$. Where source is S and pixel surface is represented by ΔS. Unit vector n_s denotes normal vector to the detector surface and u_s is the vector that goes through from source to pixel center. Also α_s is the angle between these vectors. Then photon number that reaches to the detector can be calculated by equation 3.3 [14]. Then ray is recalculated for next position in the detector until it reaches all point in the detector. At the end of the simulation for current source position, image is formed. Later, source position is changed to next location and new image data is created. Detailed flow chart for x-ray simulation is shown in Figure 3.3.

$$
\begin{aligned}
N_s(E) &= N_s^0(E) \cdot \Delta\Omega \prod_{mt} e^{-\mu_{mt}(E)\cdot x_{mt}} \\
&= N_s^0(E) \cdot \Delta\Omega \cdot e^{\left(\sum_{mt}(-\mu_{mt}(E)\cdot x_{mt})\right)}
\end{aligned}
\tag{3.3}
$$
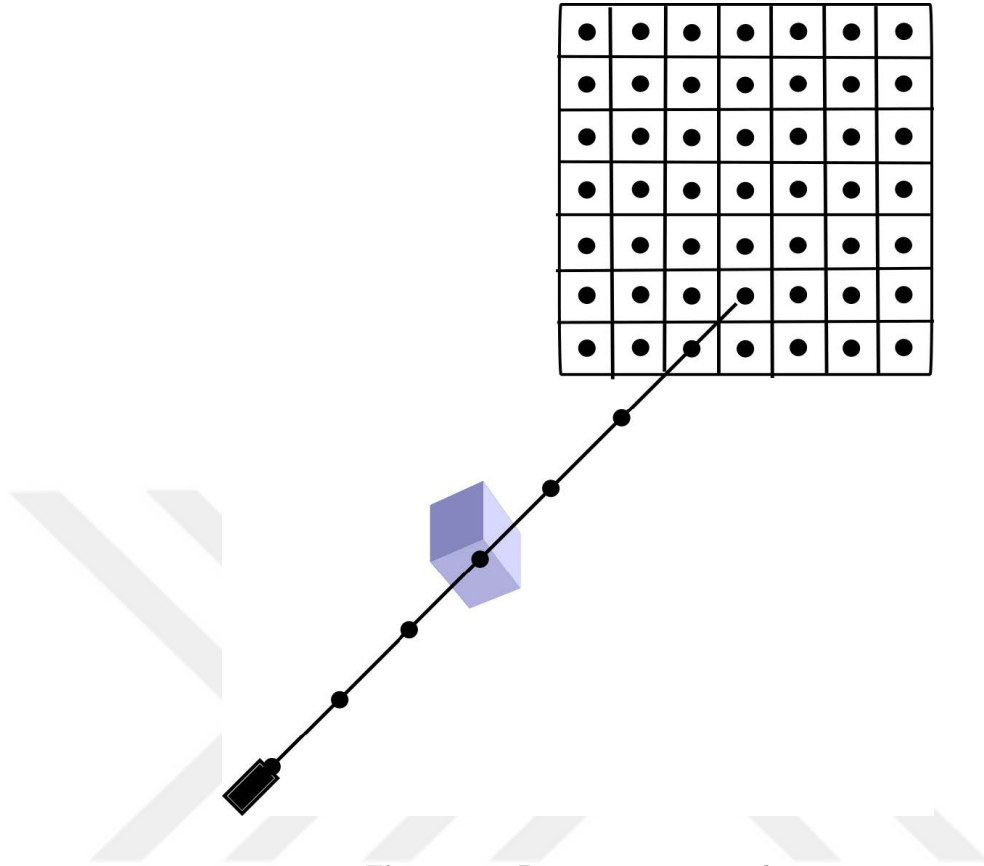
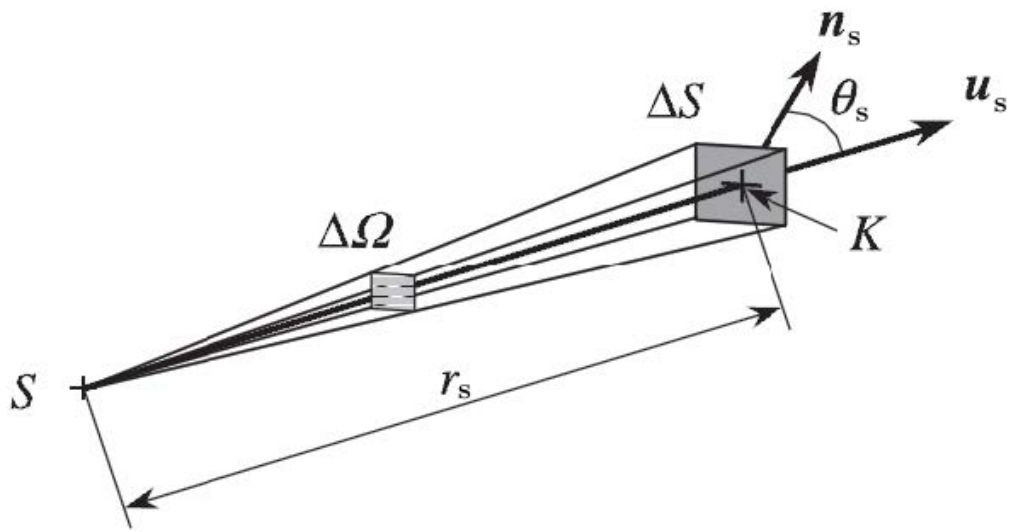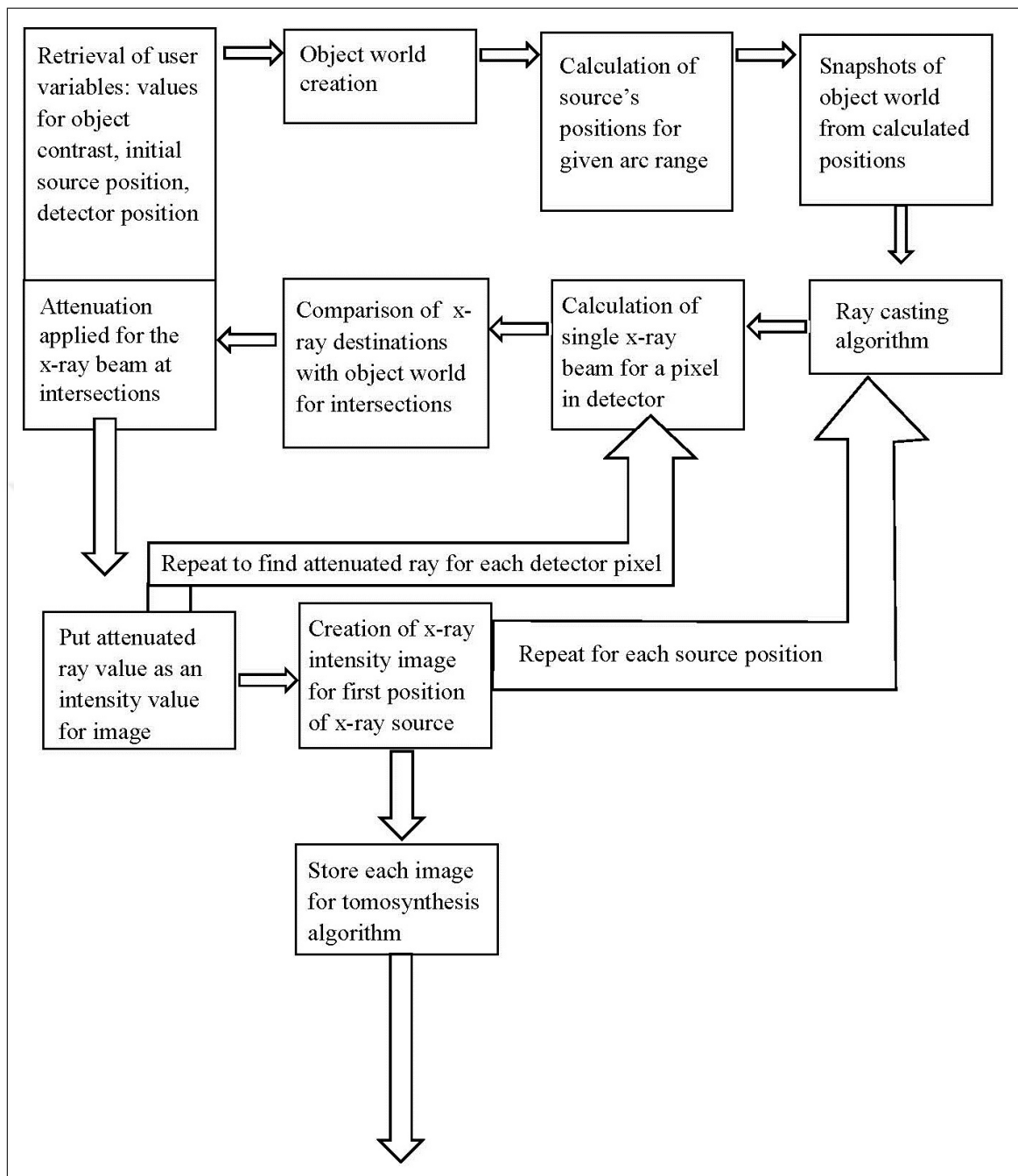**Figure 3.1** Data points in x-ray line.

Figure 3.2 Solid angle ray. Adapted from [14].

```
Retrieval of user          Object world          Calculation of         Snapshots of
variables: values    ⇒     creation          ⇒  source's            ⇒  object world
for object                                       positions for          from calculated
contrast, initial                                given arc range        positions
source position,
detector position

Attenuation          ⇐     Comparison of x-   ⇐  Calculation of      ⇐  Ray casting
applied for the            ray destinations      single x-ray           algorithm
x-ray beam at              with object world     beam for a pixel
intersections              for intersections     in detector
```

Repeat to find attenuated ray for each detector pixel

```
Put attenuated             Creation of x-ray
ray value as an      ⇒     intensity image         Repeat for each source position
intensity value            for first position
for image                  of x-ray source

                           Store each image
                           for tomosynthesis
                           algorithm
```

Figure 3.3 Flow chart for x-ray simulation algorithm.

As seen in the chart, firstly values for object contrast, initial source position, detector position and objects positions are specified. Later, object world is created based on positions given and then source positions are calculated. These positions are visualized by taking snapshots (Figures 3.4, 3.5, 3.6 and 3.7). Then ray casting algorithm starts. Points in x-ray line are found and compared with object world for

possible intersections. If intersections exist, attenuation is applied. When all points in single x-ray line is finished, intensity value is registered to corresponding image pixel. Then same calculation is repeated for each detector pixel. When all pixels are registered, image is stored for tomosynthesis application. After that same procedure is repeated for next source position. This is a basic x-ray simulation based on line equation. Time of simulation depends on size of object world and number of data points in x-ray line.

3.2   Phantoms

3.2.1   Phantom for simulated images

A virtual phantom for simulations was created to test tomosynthesis algorithm before imaging with the physical phantom. This virtual phantom consists of rectangular solids with different widths. Figures 3.4, 3.5, 3.6, 3.7 show the snapshots of the simulation data. In each column, widths of objects increases and attenuation coefficient changes through each row. Random objects was placed around these objects. These are higher contrast objects. They were placed to simulate artifacts and blur at out of plane. Small points in Figure 3.4 represent the positions of source for different positions. In this system, source moves between in an arc $\pm$ 30 degrees around isocenter with step 2 degrees. Point of views from source position at -30, 0 and +30 degrees are shown in Figures 3.5, 3.6, 3.7.
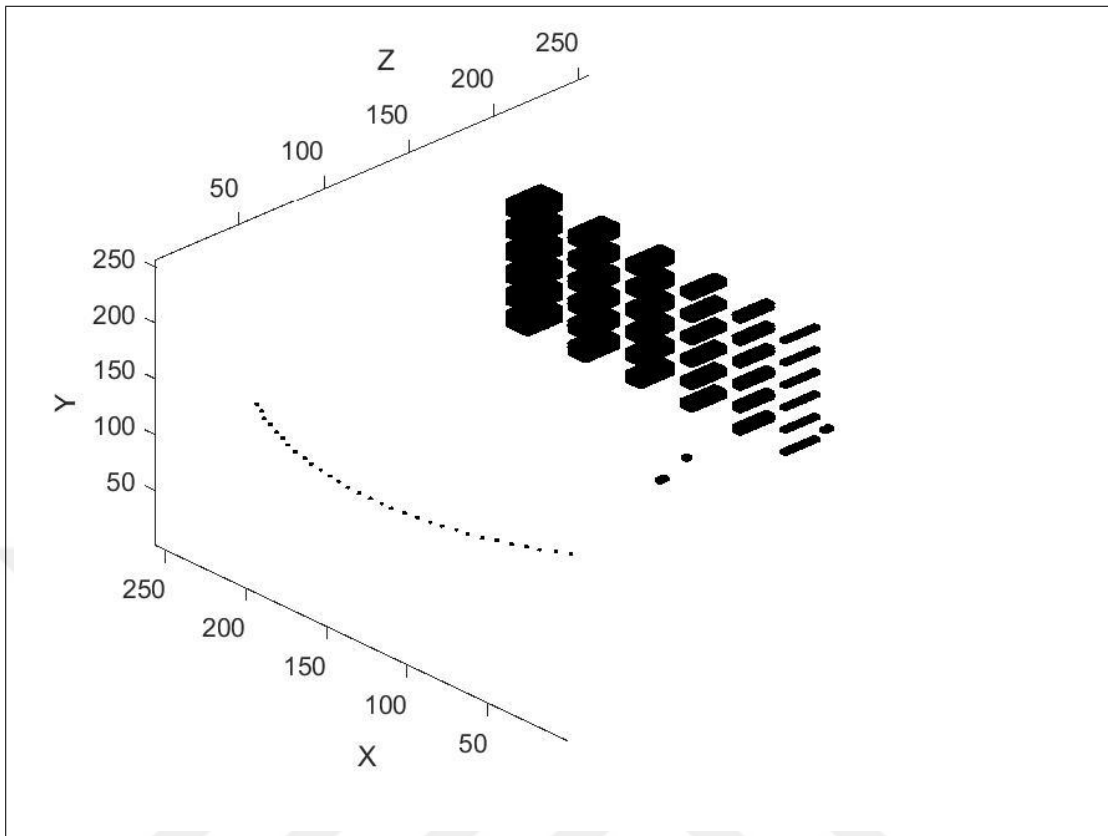
Figure 3.4 Simulation phantom.
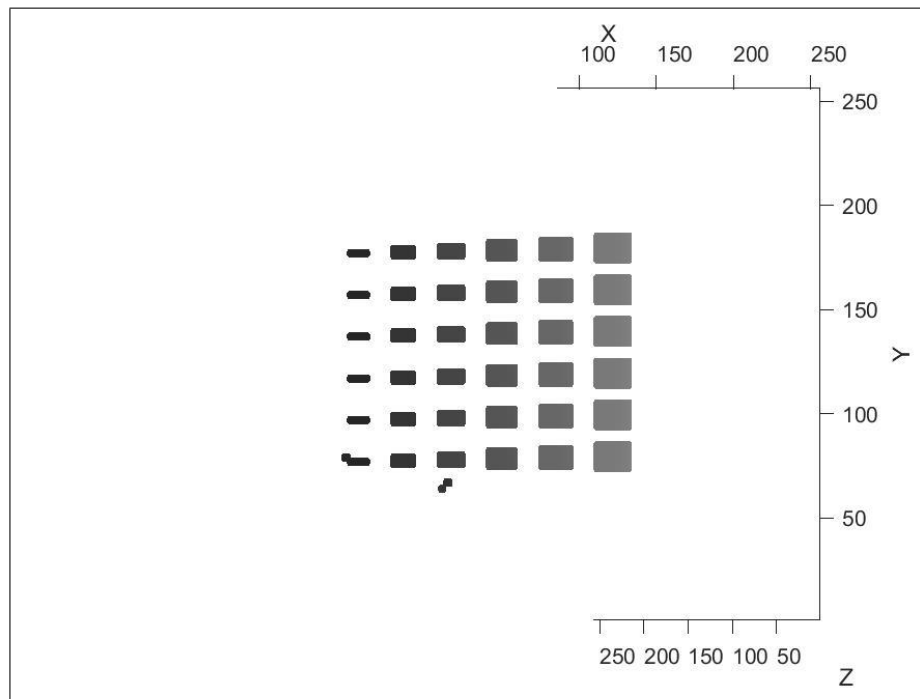
Figure 3.5 Source's point of view for simulation phantom at angle -30 degree.
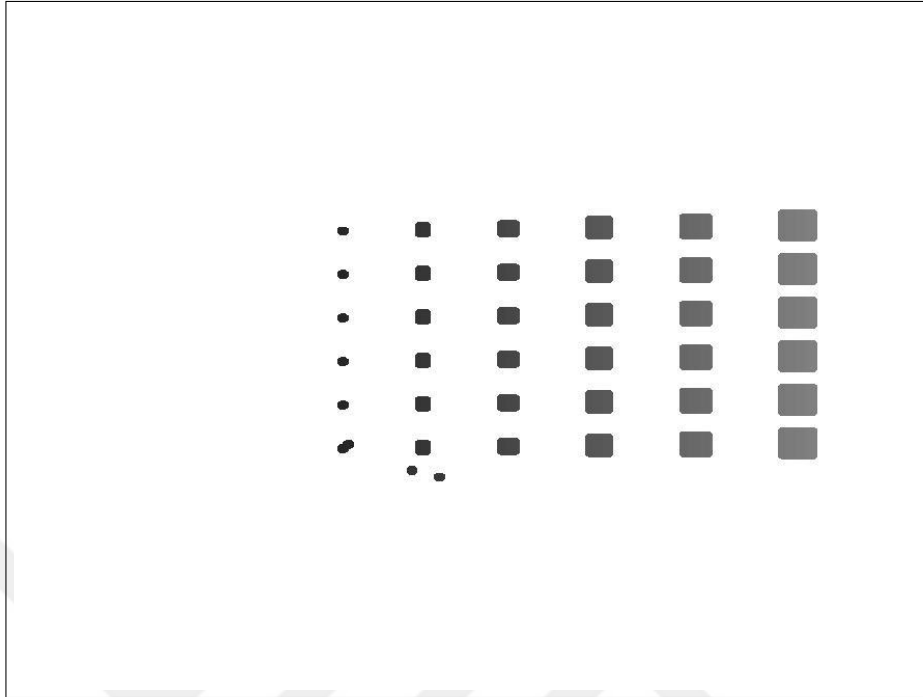
Figure 3.6 Source's point of view for simulation phantom at angle 0 degree.
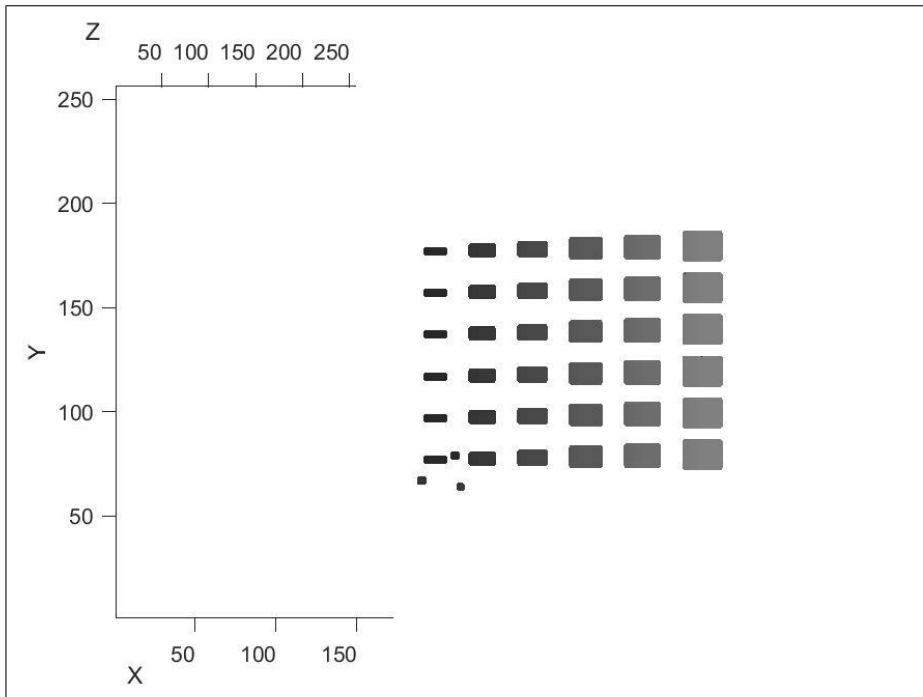
Figure 3.7 Source's point of view for simulation phantom at angle +30 degree.

3.2.2 Physical phantom for x-ray imaging

Physical phantom was created to test real world results for tomosynthesis algorithm. Since it was previously shown that epoxy could be used as a phantom material [15], epoxy was selected as the main material for objects. As seen in schematic of the physical phantom in Figure 3.8; bottom cylinder has a radius 8 cm and thickness 3.3 cm. Thickness reduces in inner circle, due to shape of the container used for molding. At the top of the epoxy cylinder, four rectangular blocks with different thickness and positions are placed. Three blocks include five by five holes. Each block have 0.7 cm, 1 cm and 1.5 cm thickness and 4.7 cm side length. Gomi [16] used $CaCO_3$ as a contrast material for phantom. In this thesis, $CaCO_3$ mixture with epoxy is used for filling holes in the rectangular blocks. As presented in Figure 3.9, holes drilled into epoxy with diameters 0.6 mm, 0.8 mm, 1mm, 1.3 mm and 1.5 mm. Then these five rows filled with epoxy-$CaCO_3$ mixture with ratio 20 mg/g, 80 mg/g, 160 mg/g, 240 mg/g, 320 mg/g. Similarly, other two block with different thickness prepared with same pattern. Last object is constituted from an epoxy block (4.7cmx2.1cmx4.7cm) and three beads with 0.9 cm diameter. All three beads are positioned at the corners of the epoxy block. Placement of objects on phantom can be seen in Figure 3.8. X-ray images were taken with GE Senographe Pristina (Figure 3.10). X-ray source rotates with an arc of approximately $\pm$ 12 degrees around isocenter. Nine images of phantom were taken at different angles.
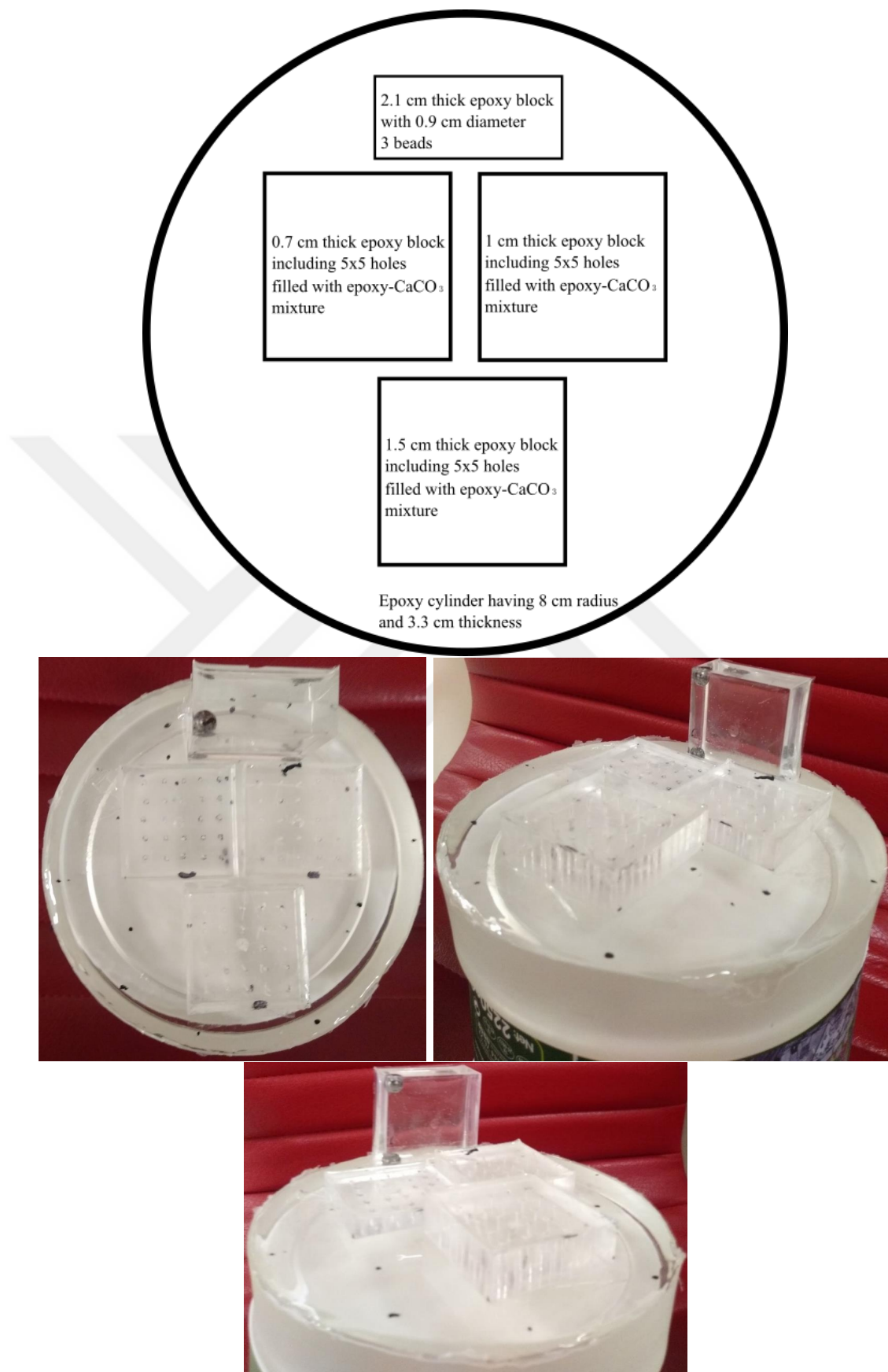
Figure 3.8 Schematic representation of physical phantom and its photographs from top and side views.

Figure 3.9 Representation of object holes.

Figure 3.10 GE Senographe Pristina [17].

3.3 Tomosynthesis

In this section, tomosynthesis technique applied in this thesis is explained briefly. Algorithm employed for tomosynthesis is based on the work of Soimu et al. [18] which is the modified version of the algorithm developed by Kolitsi et al. [1]. Therefore, both of the studies are explained in this section.
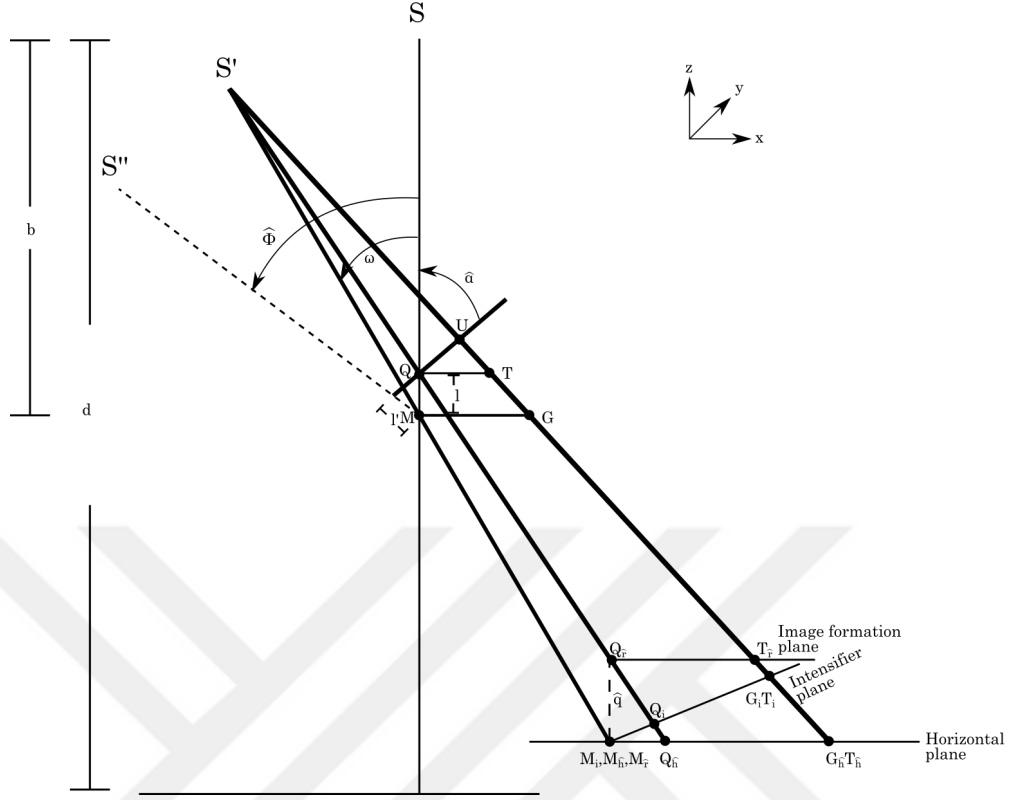
Reconstruction method used for tomosynthesis image is multiple projection algorithm (MPA). MPA method is developed by Kolitsi and colleagues. MPA technique is designed for the use of isocentric fluoroscopic units. Algorithm can able create tomosynthesis image of the selected planes with different orientation and distances from isocenter [1]. Figure 3.11 below show the schematic for the image reconstruction. Tube and image intensifier rotates around the isocenter point M. Plane at isocenter is represented by MG line. Then M_iG_i represents the acquired image of MG on the receptor for specific angle of the tube and detector. Projection of this image is shown with $M_{\hat{h}}G_{\hat{h}}$ line. Image formed on the receptor need to be transformed into projected data by

$$\hat{h} = \frac{i \cdot d}{d \cdot \cos \omega - i \cdot \sin \omega} \tag{3.4}$$

$\hat{h}$ is found by measuring the distance between horizontal projection plane $(M_{\hat{h}})$ and origin M. Similar to $\hat{h}$, "i" is equal to the displacement of image receptor plane (M_i) from origin M. This equation shows the expansion of image through x direction. Size of $M_{\hat{h}}G_{\hat{h}}$ does not change with different angle (ω). Also there is no distortion which may occur with the change in angle [2].

When focus plane is not in the plane of the isocenter, more detailed calculation is required. In Figure 3.11, image of a plane QT with a distance "l" between isocenter is shown.

Figure 3.11 Design for tomosynthesis reconstruction with multiple projection algorithm. Adapted from [1].

According to this method, transformation between image receptor and horizontal plane should be calculated for plane QT. Then projection image should be shifted according to the size of $M_{\hat{h}}Q_{\hat{h}}$. Then this data should be adjusted for different angles.

$$\hat{r} = \left(\hat{h} - \frac{l \cdot d \cdot \sin \omega}{b \cdot \cos \omega - l} \right) \cdot \left(1 - \frac{l}{b \cdot \cos \omega} \right) \tag{3.5}$$

$\hat{r}$ is the location of the modified image plane $Q_{\hat{r}}T_{\hat{r}}$. Length of plane $Q_{\hat{r}}T_{\hat{r}}$ is same with different tube position angle. Therefore, projection image processed by equations can be added to acquire desired structures of focus plane QT [2].

Another variable for reconstructed plane selection is angle $\hat{\alpha}$ with respect to x axis. When chosen plane for tomosynthesis has angle $\hat{\alpha}$, horizontal plane composition

can be reached by turning coordinate system with respect to y axis by an angle $\hat{\alpha} - 90°$. As seen in Figure 3.11, QU is positioned with an angle $\hat{\alpha}$ from vertical z axis and it is has a distance l from the isocenter. If coordinate system rotates with an angle $\hat{\alpha} - 90°$, new position of source will be $S"$. Then, selected plane will be horizontal. In new rotated system, distance l will become $l \cdot \sin \hat{\alpha}$ and angle $\hat{\phi}$ will change to $\hat{\alpha} - 90°$. Equations 3.6 and 3.7 shows the updated version for rotated plane [1].

$$\hat{r} = \left(\hat{h} + \frac{l \cdot d \cdot \sin \hat{\alpha} \cdot \cos(\omega + \hat{\alpha})}{b \cdot \sin(\omega + \hat{\alpha}) - l \cdot \sin(\hat{\alpha})} \right) \cdot \left(1 - \frac{l \cdot \sin \hat{\alpha}}{b \cdot \sin(\omega + \hat{\alpha})} \right) \tag{3.6}$$

$$\hat{h} = \frac{i \cdot d}{d \cdot \sin(\omega + \hat{\alpha}) + i \cdot \cos(\omega + \hat{\alpha})} \tag{3.7}$$

Lastly, selected plane could be selected when it has angle $\hat{\beta}$ with y axis. In this selection, it is needed prior calculation to adapt horizontal approach. Because, when plane is selected has an angle, columns of the selected plane will have different distance from the isocenter. When j^* is described as row of the x-ray image on intensifier plane, firstly row j^* needed to relocate to the plane parallel to image formation plane. Variable k shows the new position but it is needed to shifted in by an amount of $\Delta \hat{h}$. Additionally, if selected plane have a distance l from the isocenter, it is necessary magnify plane for reconstruction [1]. Resulting data can be processed with a horizontal plane approach. Equations described above can be written as follows [1]

$$k = \frac{j^* \cdot d}{j^* \cdot \cos \hat{\beta} + d \cdot \sin \hat{\beta}} \tag{3.8}$$

$$\Delta \hat{h} = \frac{M_k \cdot d \cdot \sin \omega}{b \cdot \cos \omega - M_k} \tag{3.9}$$

$$l_k = \frac{(b - l) \cdot k \cdot \cos \hat{\beta}}{d} \tag{3.10}$$

$$\hat{u} = \frac{b - l}{b} \tag{3.11}$$

$$r_o = (k - \Delta \hat{h}) \cdot \hat{u} \tag{3.12}$$

Notice that in stationary system horizontal plane is already acquired. So, calculation of horizontal plane is not performed. After acquiring data from multiple projection algorithm, image needed to be shifted and magnified to adapt stationary detector system. Variable m_{st} is the magnification ratio for selected plane to be projected onto isocenter plane. Shift required for tomosynthesis system is s_{st}. Similar to multiple projection algorithm, b is the positional difference between source to isocenter and d denotes the detector to source distance. Also l shows interval between the reconstructed plane and isocenter. Angle ω represent the angle between source and vertical axis. Lastly, angle $\hat{\alpha}$ changes if selected plane has an angle with vertical axis. Both of variables m_{st} and s_{st} can be calculated as equations described below [18].

$$m_{st} = \frac{d}{b - l} \cdot \frac{b \cdot \sin(\omega + \hat{\alpha}) - l}{b \cdot \sin(\omega + \hat{\alpha})} \tag{3.13}$$

$$s_{st} = \frac{l \cdot (b \cdot \sin(\omega + \hat{\alpha}) + d - b)}{(b \cdot \sin(\omega + \hat{\alpha}) - l) \cdot \tan(w + \hat{\alpha})} \qquad (3.14)$$

3.4 Removal of outer planes

Tomosynthesis systems are susceptible to blur and artifact due its calculation method. As explained above tomosynthesis image is acquired by addition of images from different angles. So, blurred and attenuated image data from other planes contributes to image formation. As a result of this mechanism, the streaking artifacts disrupts the reconstructed image. For this reason, information from blur and artifact inducing planes should be removed for improvement in image quality [19]. Kolitsi et al. [19] suggest a technique for removing out of plane information from the focused plane. This is achieved by repositioning plane that causes artifacts to the selected plane for mask subtraction (Figure 3.12). It is mentioned above that image projected on intensifier plane is shifted and magnified to acquire tomosynthesis image for selected plane. For structure removal, distortion inducing planes needed to be projected on image formation plane similarly. Then, tomosynthesized image needed to be processed in reverse order. That means, acquired matrix after shift and magnify operations will be applied backwards for each source's position angle to reproduce images at image formation plane. Next step in removal process is projection of these images based on the focused plane. Shifting distance and magnification factor is determined by the selected plane and applied on the distortion inducing backprojected planes. After creating all distortion inducing planes, data can be created by collecting all information from the planes with unwanted structures. Where I_{NP} and I_{SP} represents tomosythesized images of distortion inducing plane and plane of interest, respectively. After reverting back the adjustment for stationary detector system, equation for this projection process can be described as follows [19]

$$\hat{h}_{NP} = \frac{\hat{r}_{NP}}{\hat{m}_{NP}} + \delta\hat{h}_{NP} \qquad (3.15)$$

$$\hat{r}_{N,S} = (\hat{h}_{NP} - \delta\hat{h}_{SP}) \cdot \hat{m}_{SP} \qquad (3.16)$$
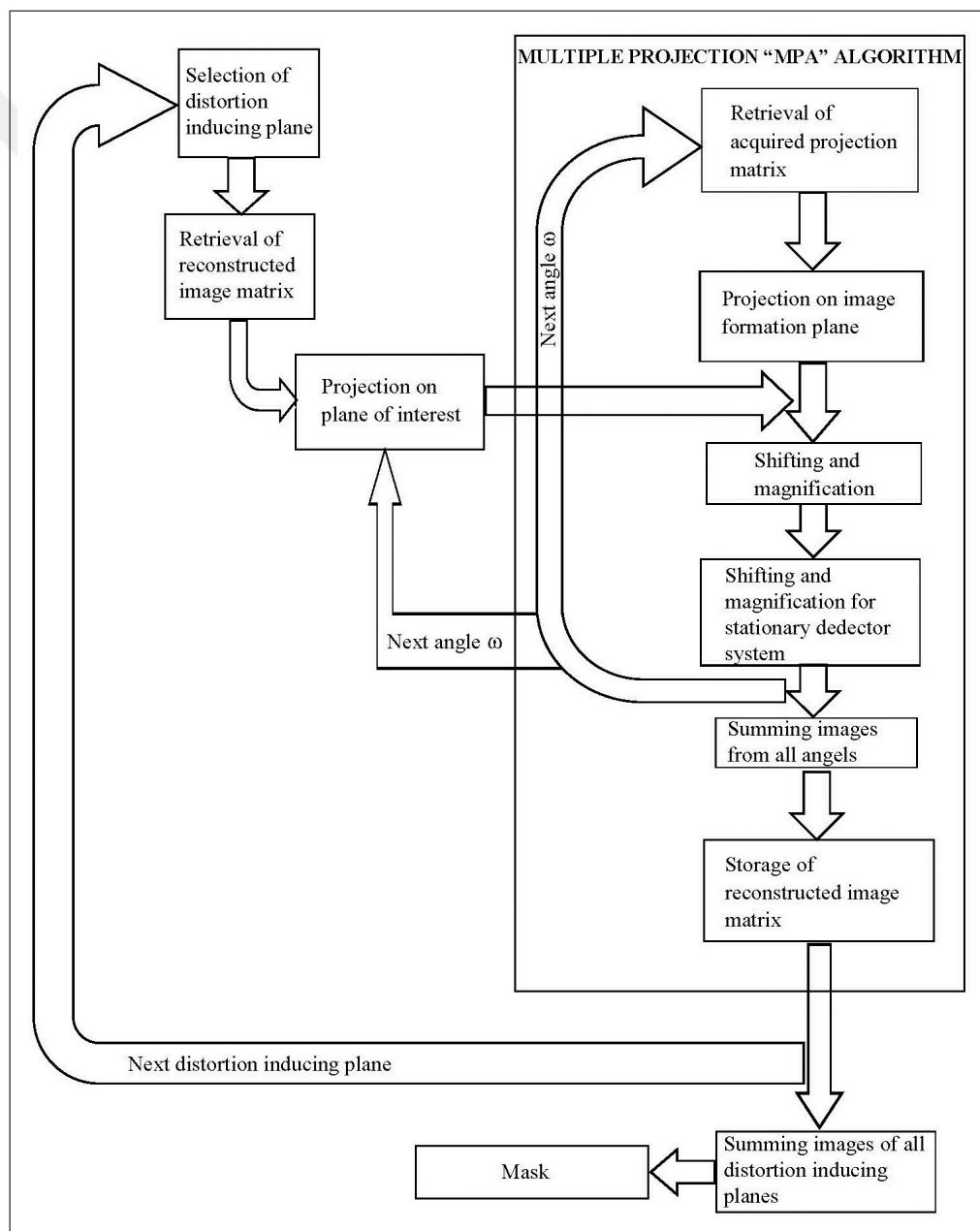
Figure 3.12 Flow chart for removal of blur and artifact procedure. Adapted from [19].

3.5 Image quality assessment

It is shown that structure similarity index (SSIM) can be used to assess the images quality[20]. Method is used to compare effect of angle range for tomosynthesis system. Widest angle range is regarded as main data for comparison. So, index between widest angle and other smaller data samples are calculated. This assessment method looks for three main variable in an image which are luminance, contrast and structure. Variables $\tau_{\acute{x}}$ and $\tau_{\acute{y}}$ represents the mean intensity value. Also, contrast is evaluated by calculation of standard deviations $\sigma_{\acute{x}}$ and $\sigma_{\acute{y}}$. Lastly, structure analyze is applied by function $(\acute{x} - \tau_{\acute{x}})/\sigma_{\acute{x}}$ and $(\acute{y} - \tau_{\acute{y}})/\sigma_{\acute{y}}$. C_1 and C_2 are the constants to prevent instability if $(\tau_{\acute{x}}^2 + \tau_{\acute{y}}^2)$ or $(\sigma_{\acute{x}}^2 + \sigma_{\acute{y}}^2)$ goes to zero. SSIM index can be given by [21]

$$SSIM(\acute{x}, \acute{y}) = \frac{(2 \cdot \tau_{\acute{x}} \cdot \tau_{\acute{y}} + C_1) \cdot (2 \cdot \sigma_{\acute{x}\acute{y}} + C_2)}{(\tau_{\acute{x}}^2 + \tau_{\acute{y}}^2 + C_1) \cdot (\sigma_{\acute{x}}^2 + \sigma_{\acute{y}}^2 + C_2)} \tag{3.17}$$

Wang et al. [21] suggested a modified approach for evaluation of images. According to this method, SSIM index should be calculated locally due to advantages over global approach. As seen equation below, $\acute{X}$ and $\acute{Y}$ represents two images to be compared. Also, $\acute{x}_{wn}$ and $\acute{y}_{wn}$ image information at local window number wn. Thirdly, Total number of local windows in image is shown with W^T. Then Mean structure similarity index can be written as follows [21]

$$MSSIM(\acute{X}, \acute{Y}) = \frac{1}{W^T} \cdot \sum_{wn=1}^{W^T} SSIM(\acute{x}_{wn}, \acute{y}_{wn}) \tag{3.18}$$

SSIM function that was used during calculations is from [22].

4. RESULTS AND DISCUSSION

4.1 X-ray images

In this chapter, firstly, x-ray simulation images are given and effect of the number of data points in x-ray line is presented. Later, projection images for different tube angles are shown (Section 4.1.1). In Section 4.1.2, x-ray images of physical phantom for different angles are given. Tomosynthesis simulation results are discussed in Section 4.2.1. Results of tomosynthesis for physical phantom is presented in Section 4.2.2. In Section 4.2.3, results of distortion inducing plane removal is presented.

4.1.1 X-ray simulation images

As written in Section 3.1, data points of the algorithm designed for x-ray simulation are changeable. Images in Figure 4.1 show the effect of number of data points in a ray. Images on the left hand side show x-ray projections of simulation when number of data points in x-ray line between source and detector pixel is insufficient. Object projections seen in these images become discrete due to inadequate distance between two data points. On the other hand, in the images on the right hand side; x-ray projections are more realistic due to increased number of data points.
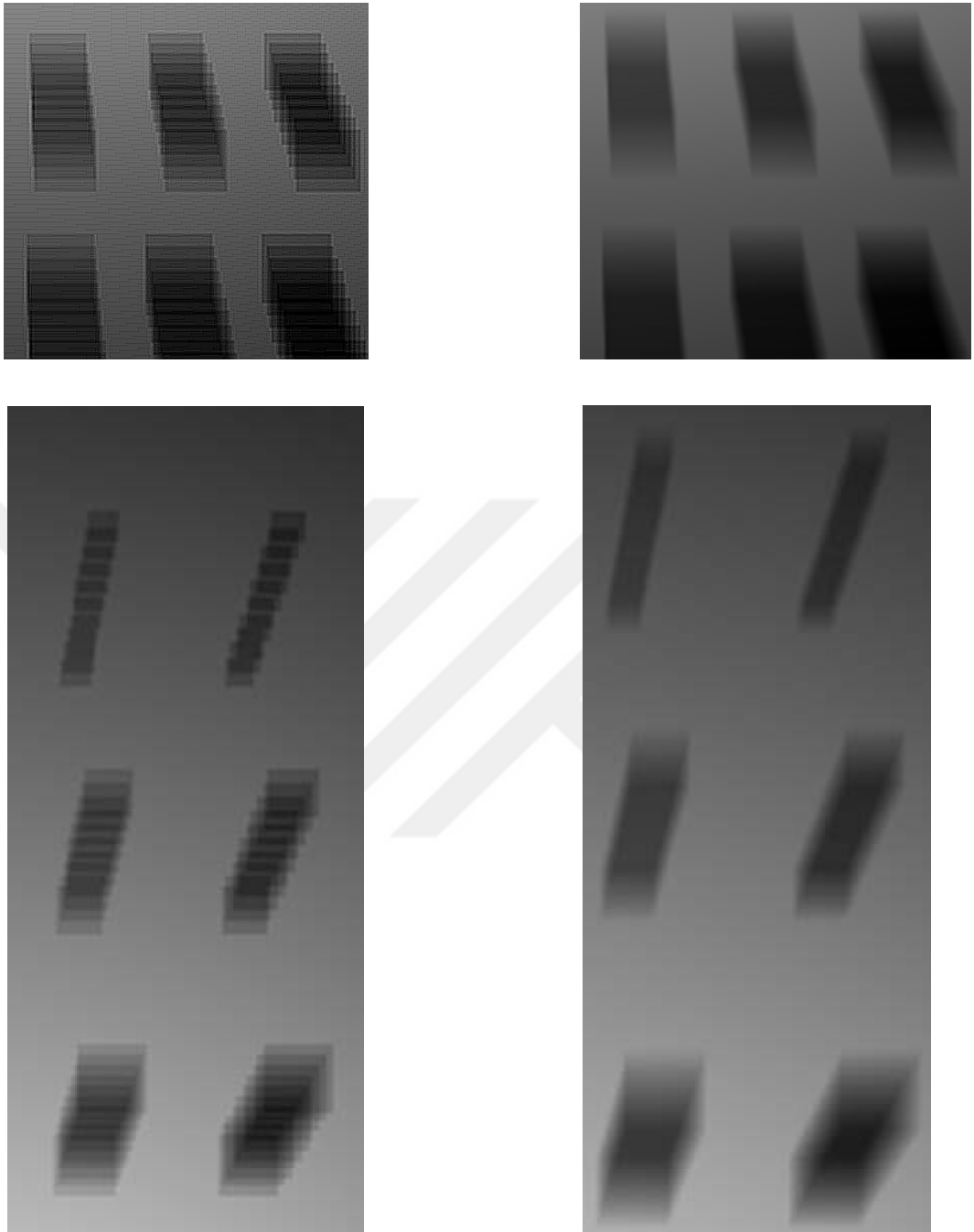
Figure 4.1 Effect of number of data points in x-ray line. Projections with insufficient points are given at left side. Projections with enough points are shown at right side.

Figure 4.2 shows phantom data for x-ray image created at a 60° arc. 31 images were simulated when x-ray source moved with step of 2°. Object positions can be seen in Figures 3.4, 3.5, 3.6, 3.7 within Section 3.2.1. Note that positions in graphics are downscaled by 2. For simulation, ratio between source to isocenter distance and source to detector is 390/502. Note also that image contrasts are adjusted for better viewing.

$-30°$	$-28°$	$-26°$
$-24°$	$-22°$	$-20°$
$-18°$	$-16°$	$-14°$
$-12°$	$-10°$	$-8°$

−6°	−4°	−2°
0°	+2°	+4°
+6°	+8°	+10°
+12°	+14°	+16°
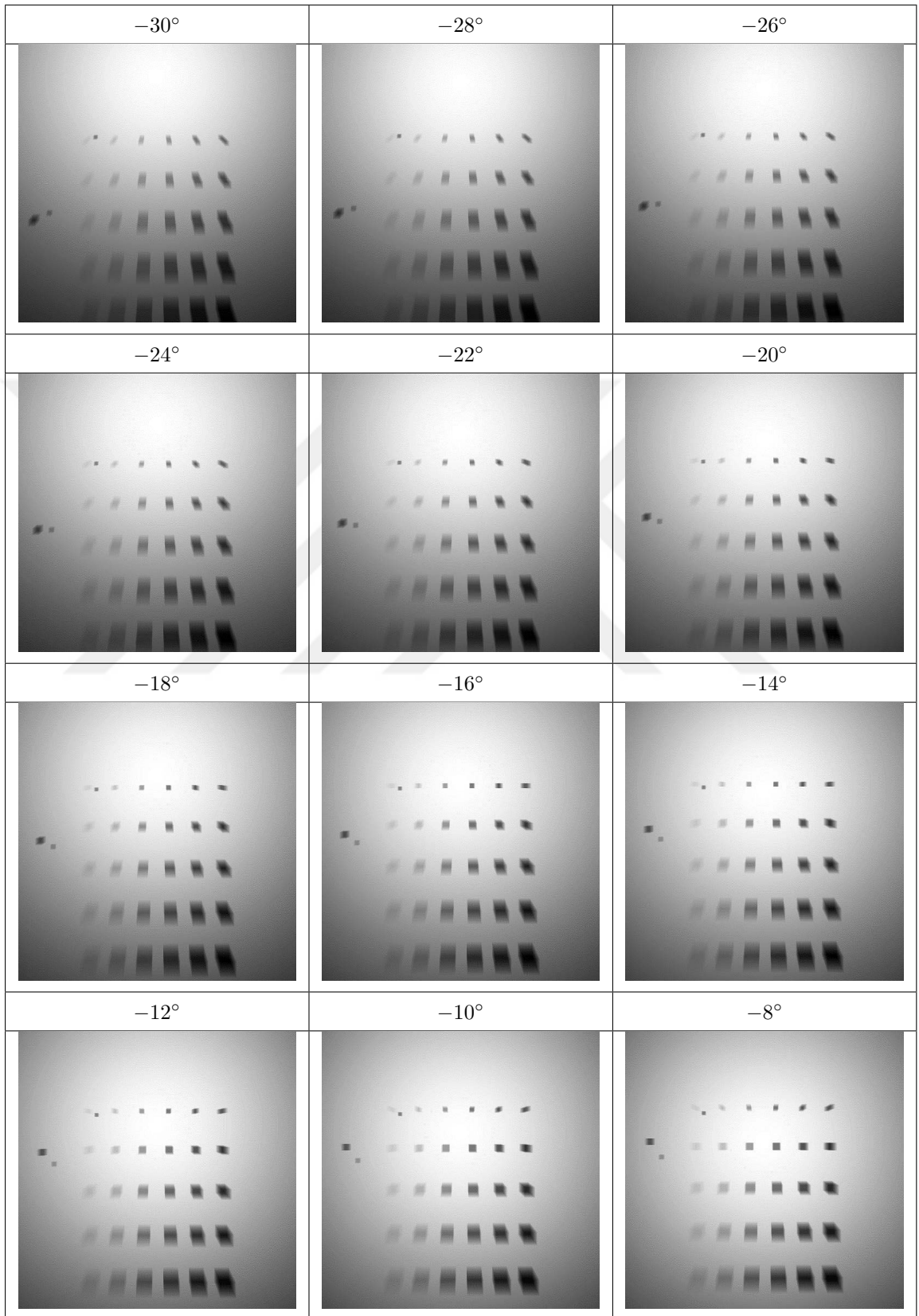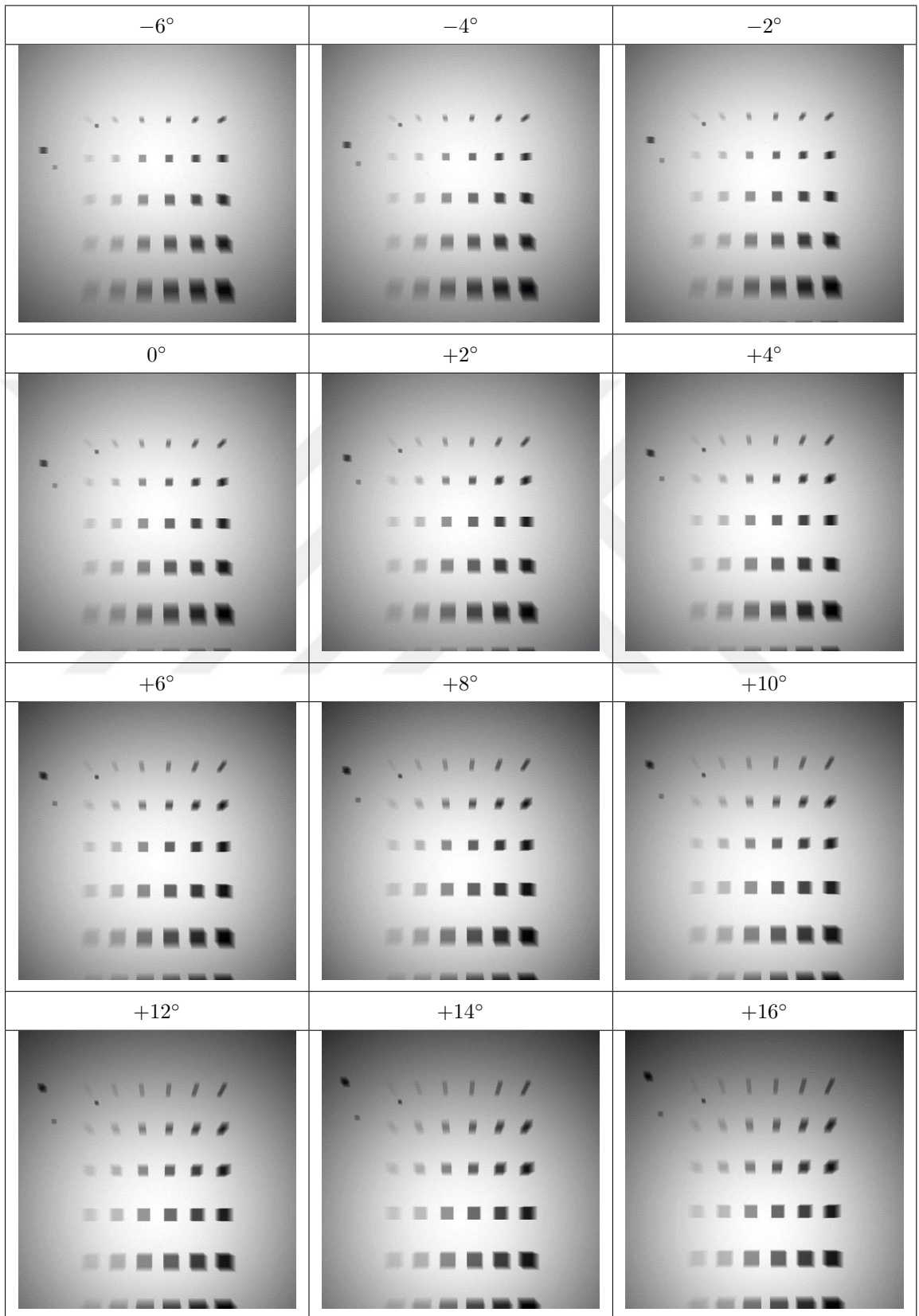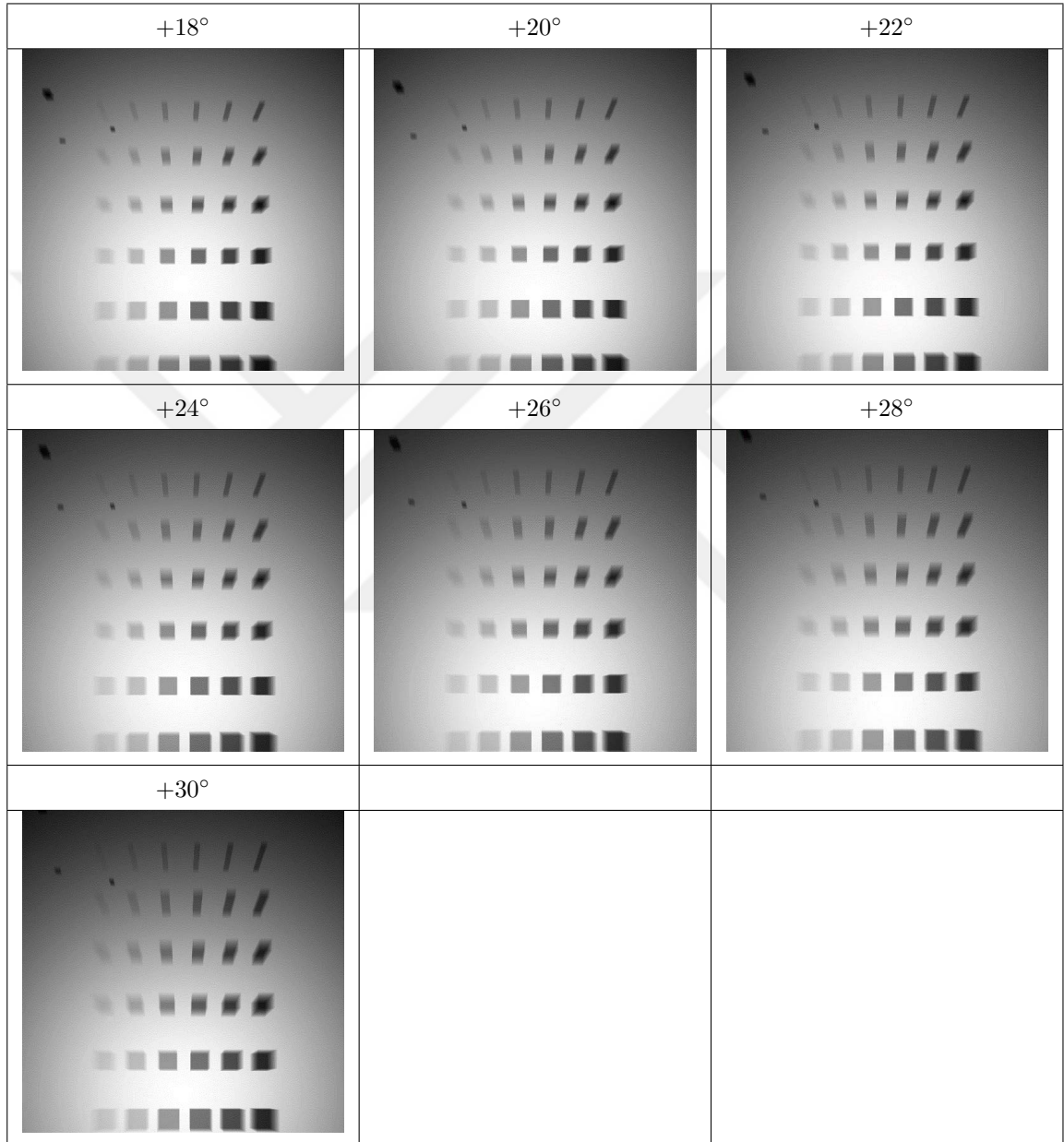
Figure 4.2 Simulated phantom images from -30 to +30 with 2 degree step.

4.1.2 Physical phantom images

Physical phantom was constructed (Section 3.2.2) to acquire real images with GE Senographe Pristina. 9 images were taken with range of 24 degrees. Distance from source to detector was approximately 660 mm. Also, source to patient distance was around 636 mm. Images taken at 34.02 kVp while exposure time and X-ray tube current were around 74 ms and 55 mA respectively. Images with corresponding angles are shown below (Figure 4.3). According to dicom conformance statement manual [23], magnification factor is SID/(SOD-20mm) where SID is source to detector and SOD represents the source to patient distances. Therefore, it is assumed that isocenter is (SOD-20mm). Images with contrast adjustment are presented in Figure 4.3.

$-0.03°$	$-2.88°$

$+5.82°$	$+8.74°$

$+11.86°$	
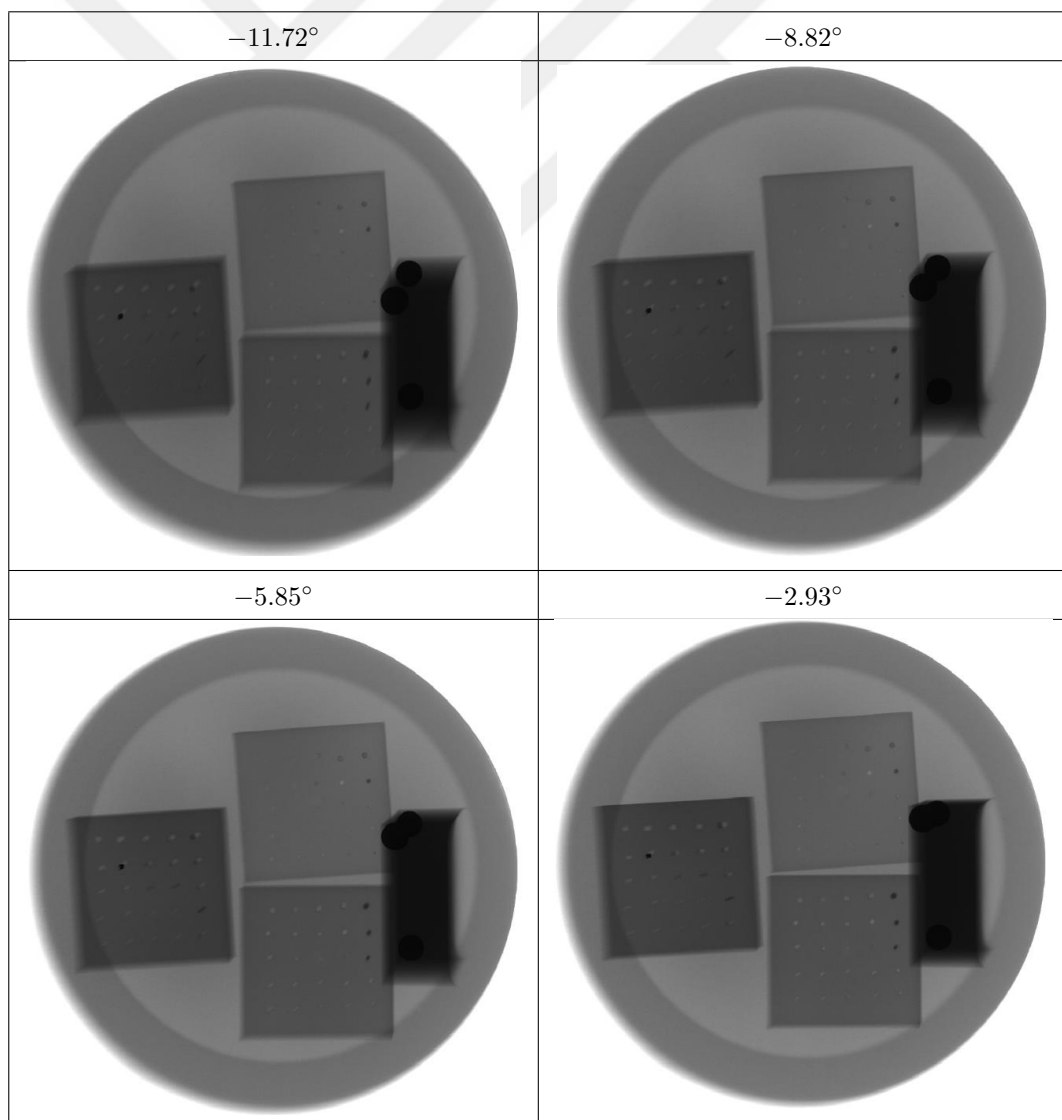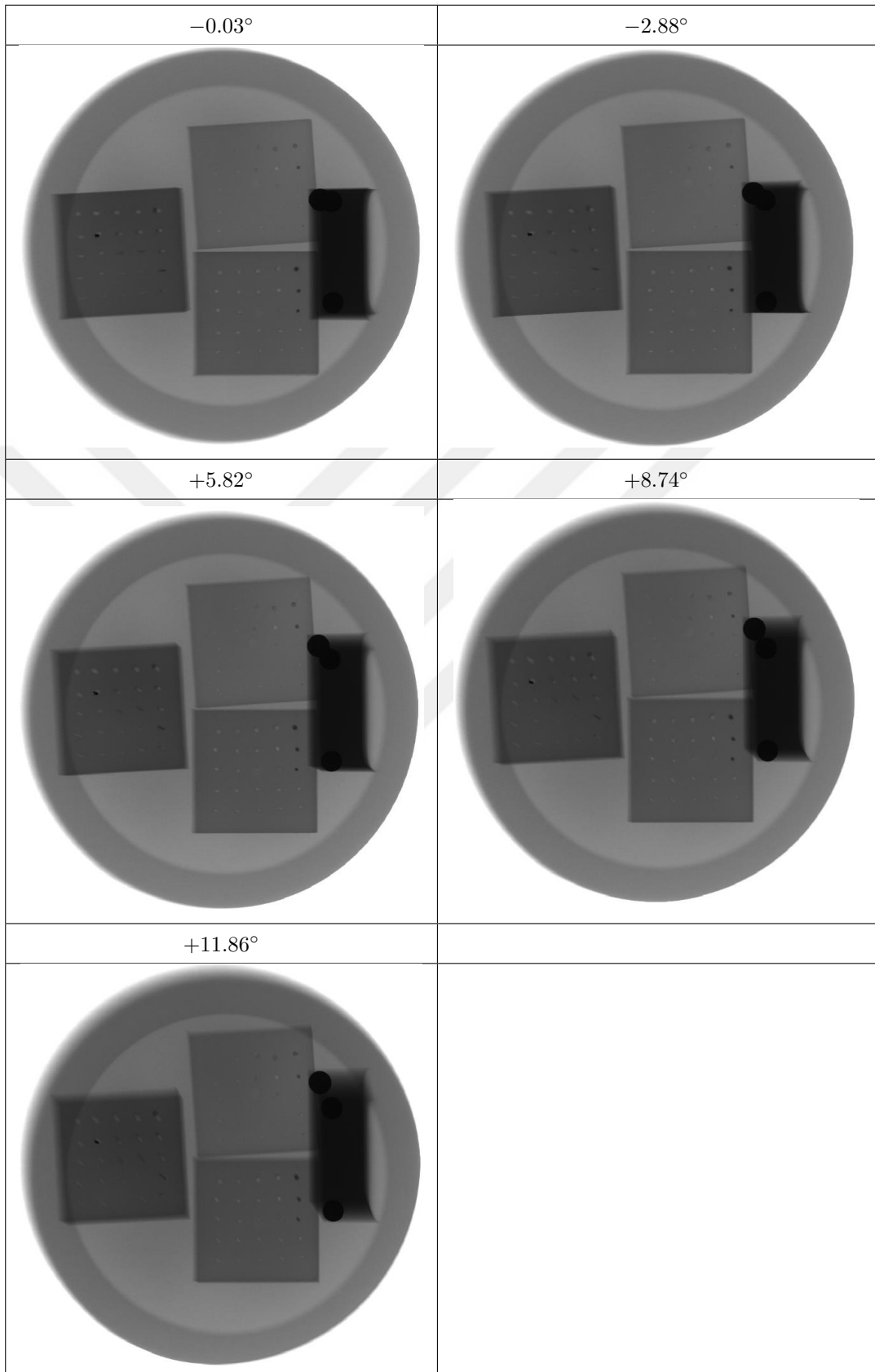
Figure 4.3 Physical phantom images from -12 to +12 with 3 degree step.

4.2 Tomosynthesis results
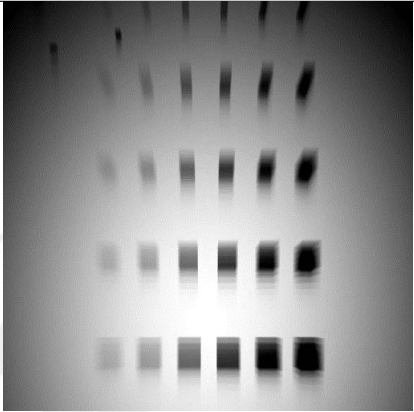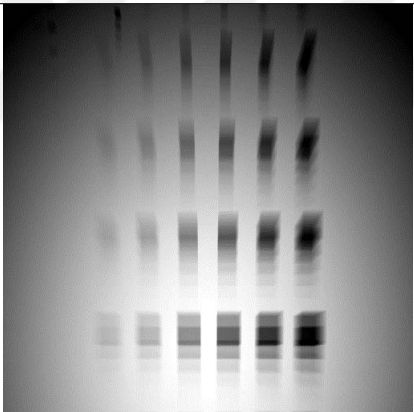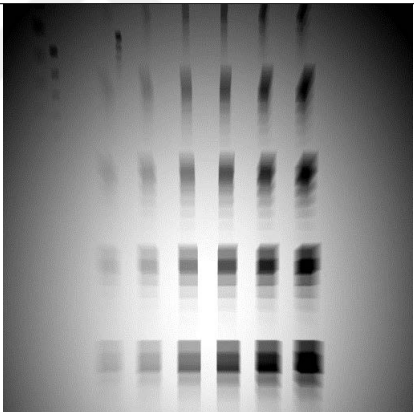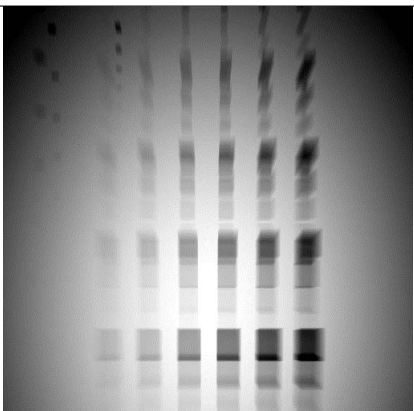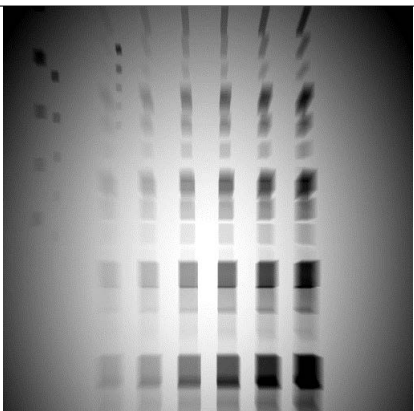
4.2.1 Tomosynthesis simulation results

Tomosynthesis algorithm explained in Section 3.3 was applied depending on five variables. First one is angle range of acquisition. Algorithm is applied an arc of 60°, 40°, 24° and 12°. Second variable is the step size in degrees. Images have angle difference 8°, 4°, 2°. Other three variables are angle $\hat{\beta}$, angle $\hat{\alpha}$ and distance l that explained in Section 3.3. 90°, 70°, 50°, 30° are selected for both angle $\hat{\beta}$ and angle $\hat{\alpha}$. 7 planes are selected for reconstruction. Selected values for distance l from isocenter were 100, 20, 0, −10, −30, −50, −80. Distances were calculated from Cartesian coordinate points. Reconstructions with single projection were only presented as image. They were not included in similarity comparisons. Highest angle arc and lowest step size used as a reference image for comparisons. List of variables selected for acquisition is given in Table 4.1.

Table 4.1
Selected parameters for variables during reconstruction process.

Acquisition arc range	Step	Distance l	Angle $\hat{\alpha}$	Angle $\hat{\beta}$
60°, 40°, 24° , 12°	8°, 4°, 2°	100, 20, 0, −10, −30, −50, −80	90°, 70°, 50°, 30°	90°, 70°, 50°, 30°

First set of tomosynthesis images were prepared while angle $\hat{\beta}$ and angle $\hat{\alpha}$ were 90°. Also distance l from the isocenter was −30. Figure 4.4 shows the reconstructed images.

Step	Range	
	60°	40°
2°		
4°		
8°		

Step	Range	
	24°	12°
2°		
4°		
8°		
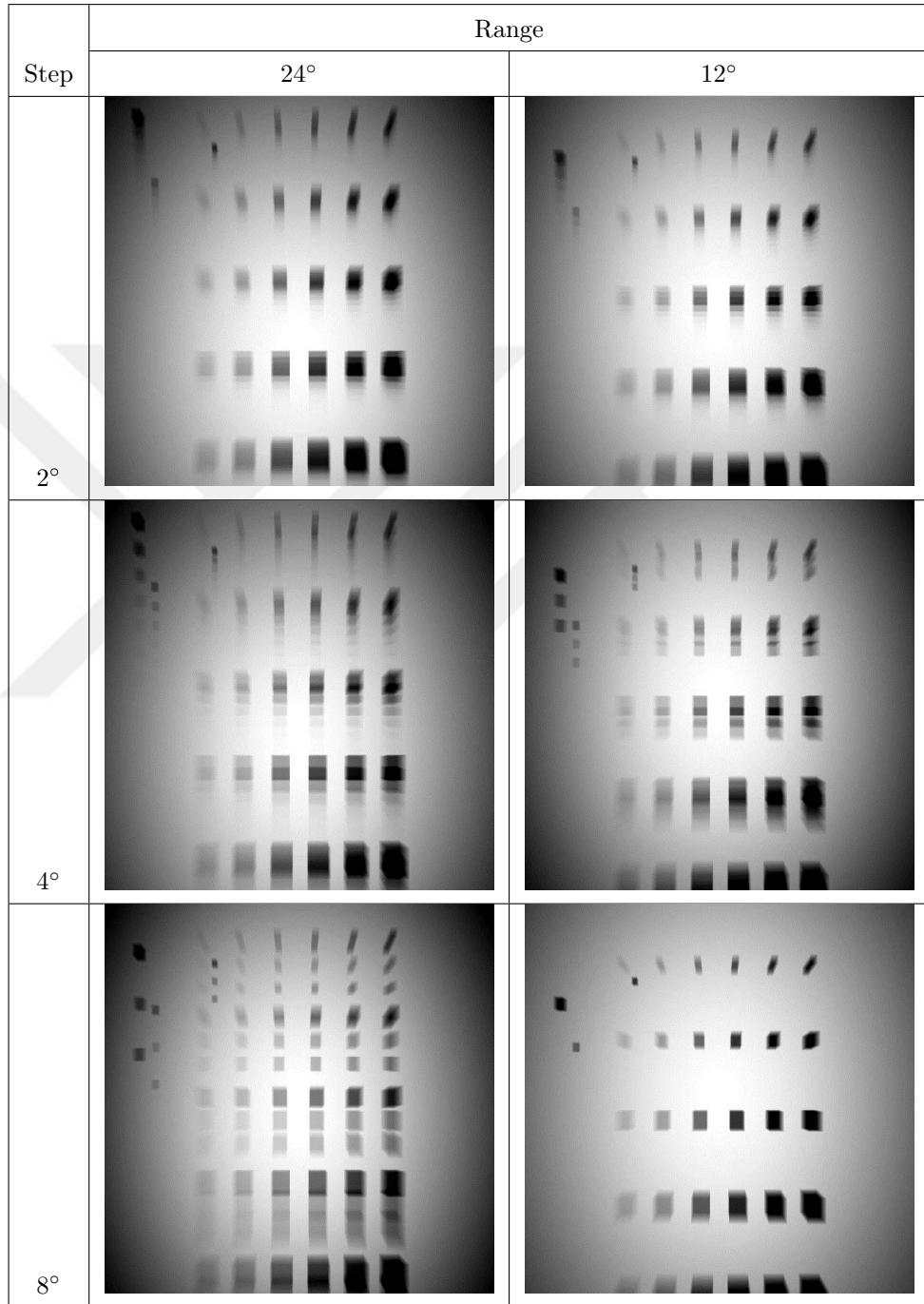
Figure 4.4 Simulated phantom reconstructed images at $l = -30$, $\hat{\beta} = 90°$ and $\hat{\alpha} = 90°$.

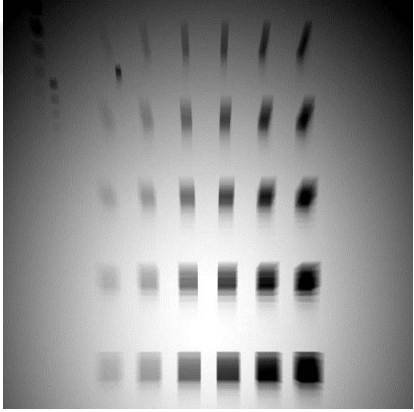Mean structure similarity (MSSIM) values are calculated for each images. Reference data was reconstructed image at 60° arc and 2° step. Figure 4.5 shows MSSIM values of tomosynthesis images.
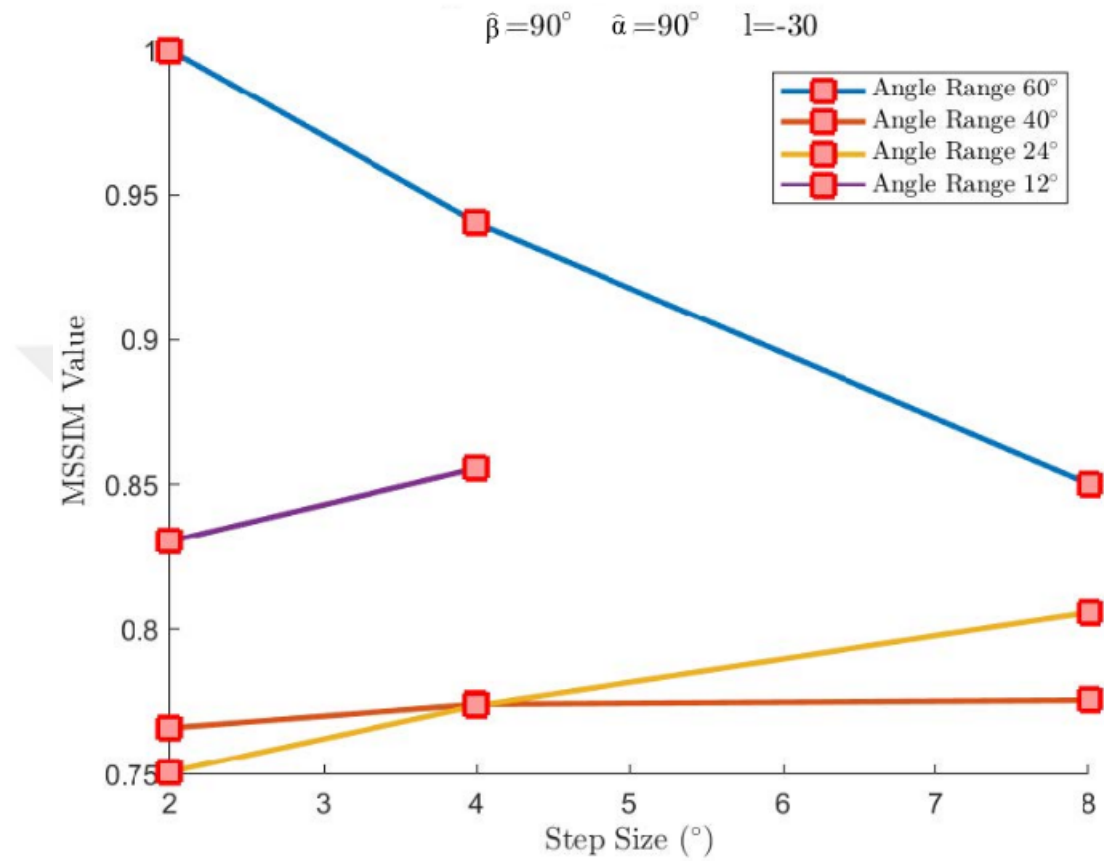
Figure 4.5 Mean structure similarity values (MSSIM) at $l = -30$, $\hat{\beta} = 90°$ and $\hat{\alpha} = 90°$.
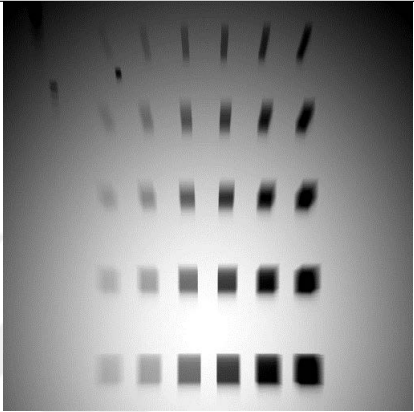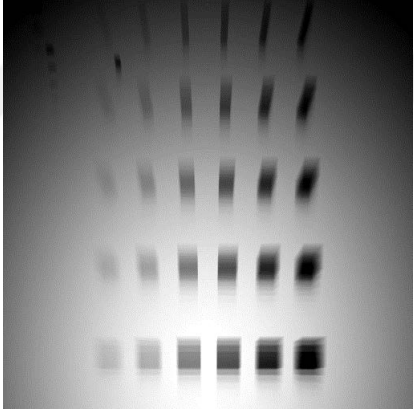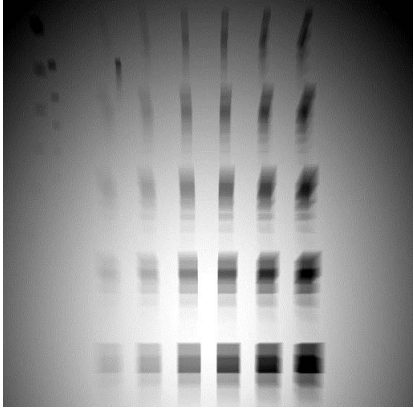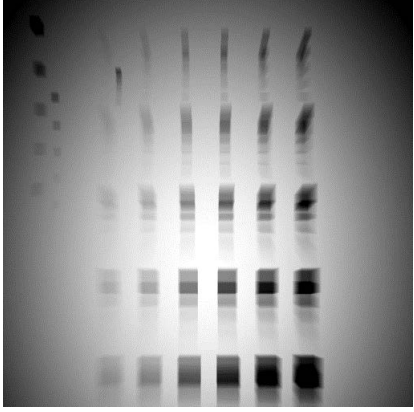
Table 4.2 shows the MSSIM values with corresponding variables for each image.

Table 4.2
Mean structure similarity values (MSSIM) $l = -30$, $\hat{\beta} = 90°$ and $\hat{\alpha} = 90°$.

| Angle Range	Step	MSSIM	Number of Projections	Actual Angle Range
60	2	1	31	60
60	4	0.9403	15	56
60	8	0.8502	7	48
40	2	0.7662	21	40
40	4	0.7744	11	40
40	8	0.7757	5	32
24	2	0.7509	13	24
24	4	0.7739	7	24
24	8	0.8059	3	16
12	2	0.8305	7	12
12	4	0.8558	3	8

Figure 4.5 shows that highest MSSIM values are achieved with 60° and 12° range. When 60° angle range images in Figure 4.4 is analyzed, ghosting becomes apparent with higher step sizes. In Table 4.2 and Figure 4.5, similarity value for 40° and 24° angle range increases with higher step sizes and lower number of projections. Reason for this could be the magnification as explained in Section 3.3. When distance l is negative, image is magnified by ratio $1 - (l/(b \cdot \cos \omega))$. Therefore, increasing image size in each projection could contribute to image distortion. Similarity for 12° range is calculated higher than 40° and 24° values where magnification factor is also plays role on higher similarity value. Additionally, higher step size could be another factor. For example, in Table 4.2, similarity value is higher for 12° range with 2° steps than 24° with 4° steps although number of projections were same for both cases.

Another set of reconstruction was applied when selected plane have an angle with x axis. Angle $\hat{\alpha}$ is set to 70°, while angle $\hat{\beta}$ kept at 90°. Also selected plane was placed at the isocenter. Reconstructed images are presented in Figure 4.6.

Step	Range	
	60°	40°
2°		
4°		
8°		

Step	Range	
	24°	12°
2°		
4°		
8°		
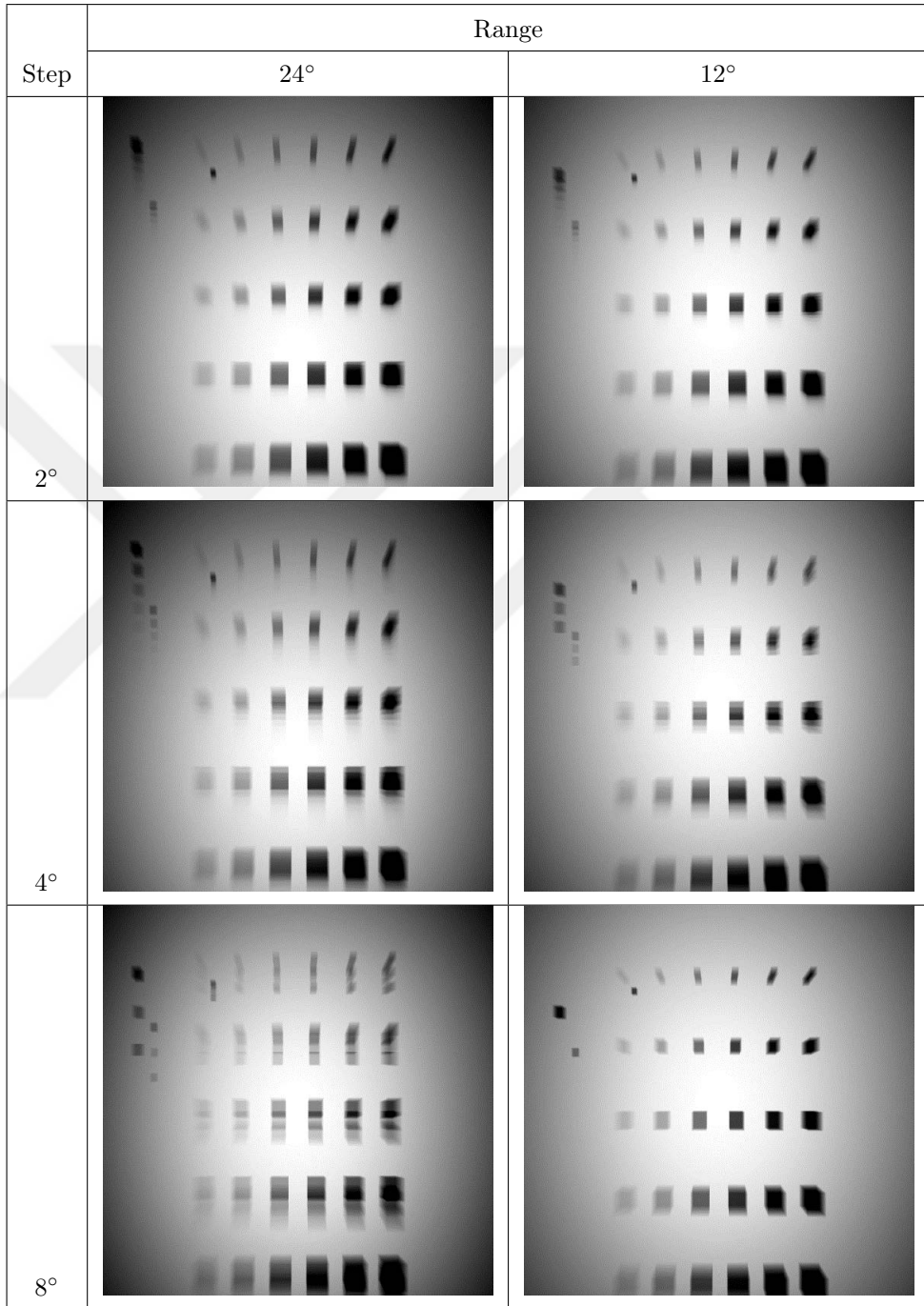
Figure 4.6 Simulated phantom reconstructed images at $l = 0$, $\hat{\beta} = 90°$ and $\hat{\alpha} = 70°$.

Also MSSIM values are calculated when $\hat{\alpha} = 70°$. Figure 4.7 shows the graph for image comparison values.
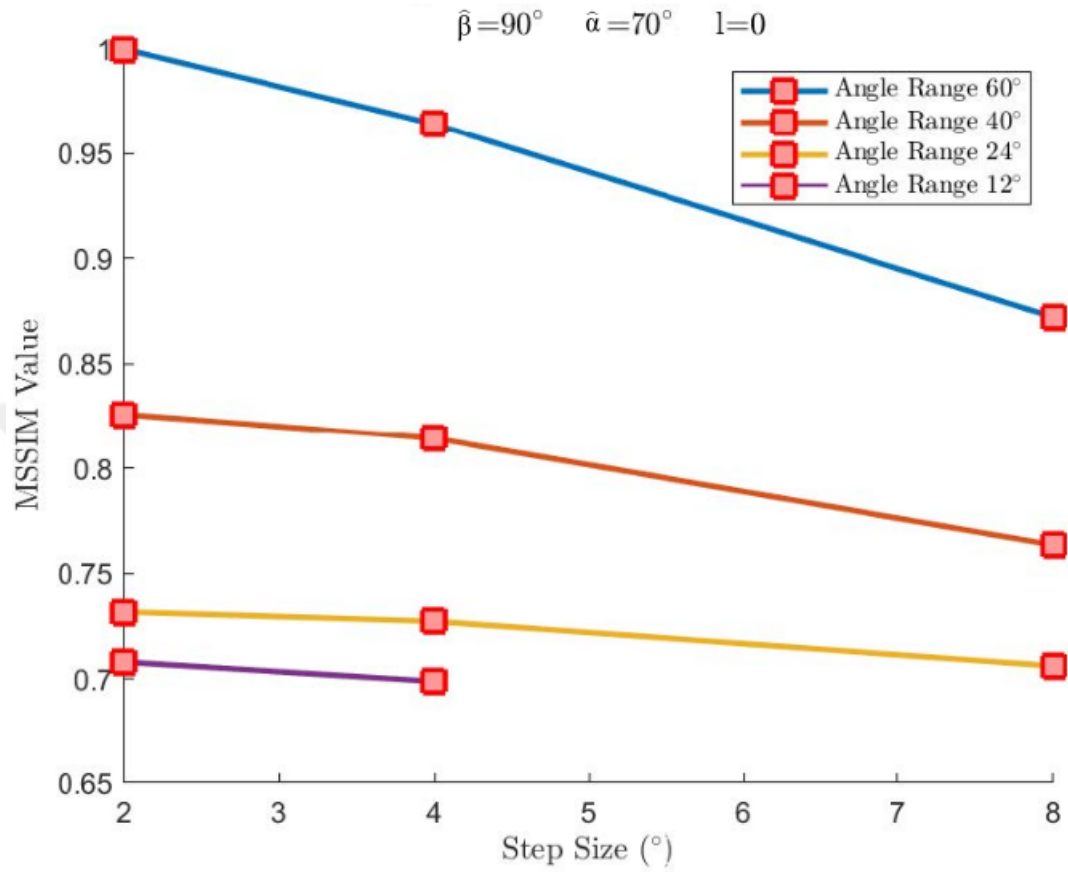
Figure 4.7 Mean structure similarity values (MSSIM) at $l = 0$, $\hat{\beta} = 90°$ and $\hat{\alpha} = 70°$.
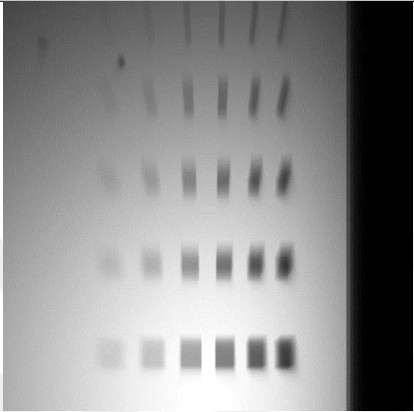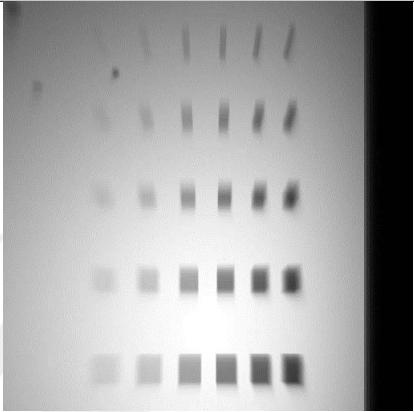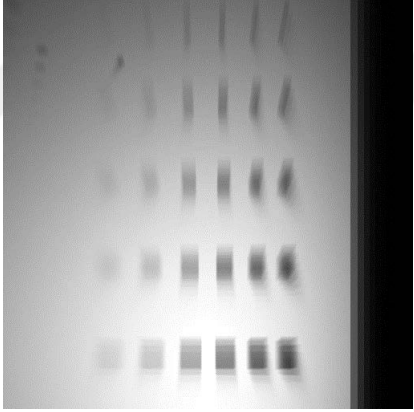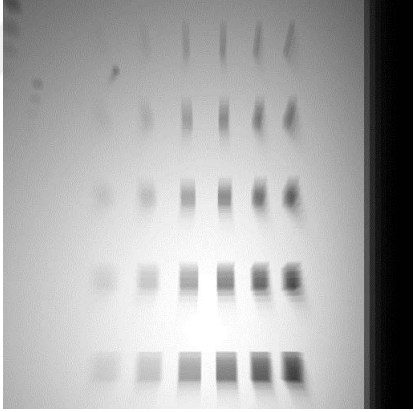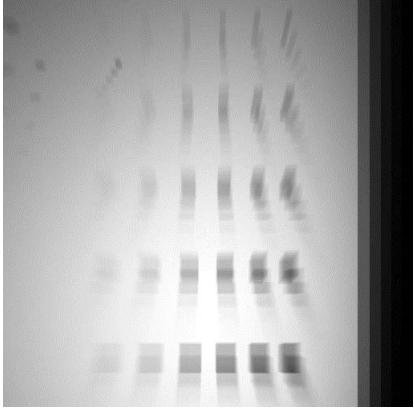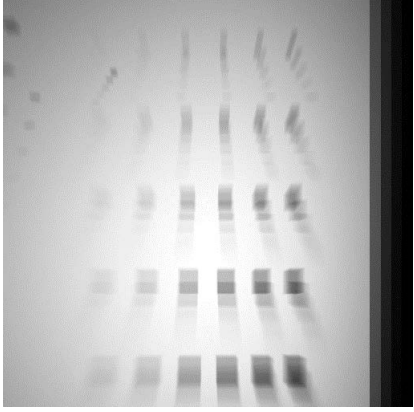
Calculated values for images difference analysis are presented in Table 4.3.

Table 4.3
Mean structure similarity values (MSSIM) $l = 0$, $\hat{\beta} = 90°$ and $\hat{\alpha} = 70°$.

Angle Range	Step	MSSIM	Number of Projections	Actual Angle Range
60	2	1	31	60
60	4	0.9642	15	56
60	8	0.8721	7	48
40	2	0.8259	21	40
40	4	0.8143	11	40
40	8	0.7634	5	32
24	2	0.7318	13	24
24	4	0.7273	7	24
24	8	0.7060	3	16
12	2	0.7079	7	12
12	4	0.6987	3	8

60° range had greater values than the other angle ranges. MSSIM values of all reconstructed images decreased with greater steps. Figure 4.7 shows that angle range is more effective than step size. For example, 60° arc with 4° steps compared with 40° arc and 2° steps; it can be seen that although 40° arc had higher number of projections, 60° arc reconstructed image with greater steps had higher similarity. Also, images with same number of projections are examined in Table 4.3. For instance, when 7 projections used for reconstruction at angle arcs 60°, 24° and 12°, similarity values decreased with lower acquisition angle range.

In the third set of images, angle $\hat{\beta}$ and angle $\hat{\alpha}$ were set to 70° and 90° respectively. Selected plane was placed at the isocenter (Figure 4.8).

Step	Range	
	60°	40°
2°		
4°		
8°		

Step	Range	
	24°	12°
2°		
4°		
8°		
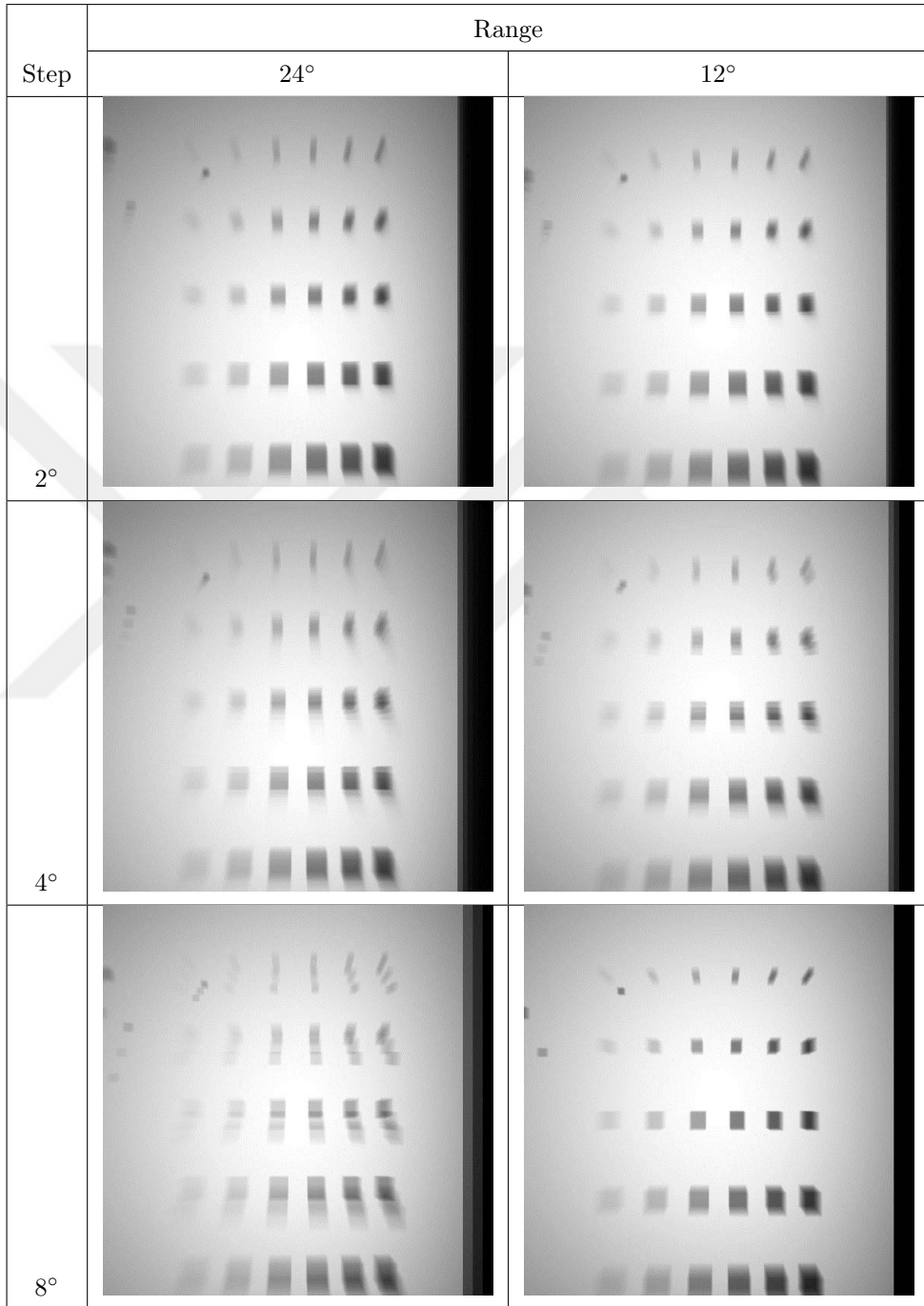
Figure 4.8 Simulated phantom reconstructed images at $l = 0$, $\hat{\beta} = 70°$ and $\hat{\alpha} = 90°$.

Similar to previous reconstructed sets, graph for MSSIM values are presented in Figure 4.9.
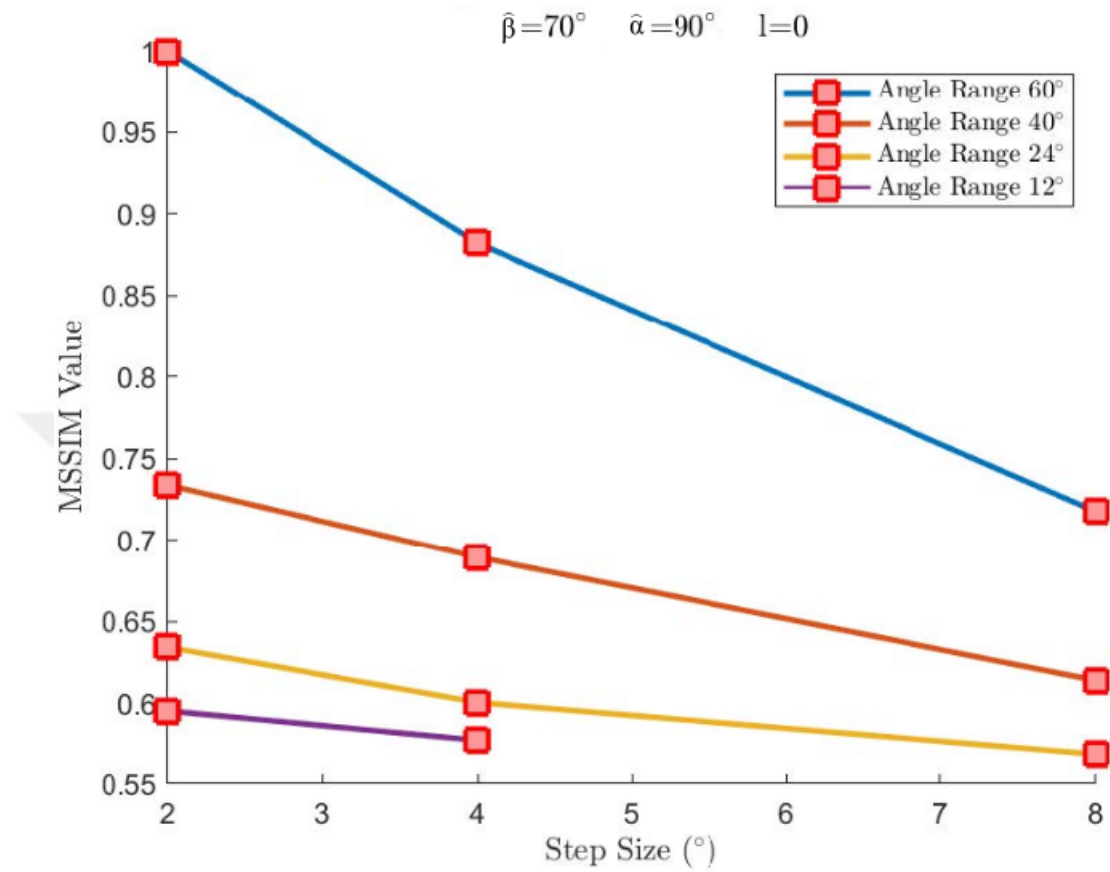
Figure 4.9 Mean structure similarity values (MSSIM) $l = 0$, $\hat{\beta} = 70°$ and $\hat{\alpha} = 90°$.

Calculated MSSIM and reconstruction properties are presented in Table 4.4.

Table 4.4

Mean structure similarity values (MSSIM) $l = 0$, $\hat{\beta} = 70°$ and $\hat{\alpha} = 90°$.

Angle Range	Step	MSSIM	Number of Projections	Actual Angle Range
60	2	1	31	60
60	4	0.8823	15	56
60	8	0.7176	7	48
40	2	0.7338	21	40
40	4	0.6893	11	40
40	8	0.6138	5	32
24	2	0.6341	13	24
24	4	0.6004	7	24
24	8	0.5688	3	16
12	2	0.5953	7	12
12	4	0.5773	3	8

In Figure 4.9, it is seen that MSSIM values showed decreasing trend with increase in step size. Comparison of Table 4.4 with Tables 4.2 and 4.3 reveals that for each case, reduction rate is higher. Table 4.2 shows that when data was reconstructed at 60° with 4° steps and 40° with 2° steps, MSSIM values calculated as 0.9403 and 0.7662 respectively. Also, similarity values were found 0.9642 and 0.8259 for same angle arcs and step sizes in Table 4.3. When angle $\hat{\beta}$ was changed, comparison values were 0.8823 and 0.7338.

Figure 4.10 shows the reconstructed images with different angles. Angle $\hat{\beta}$ and angle $\hat{\alpha}$ were both set to 30°, 50°, 70° and 90°. Angle arc was 60° and angle step size was 2° for this process. It is seen that lower angle $\hat{\beta}$ values distorts image considerably. When 30° and 50° reconstructions were observed, focus plane is created with incomplete information. Kolitsi et al. [1] points out that angle value needs to be higher than 60° for sufficient reconstruction of selected plane since tube rotates in only x-z axes. Also, angle $\hat{\alpha}$ could affect the reconstruction process. When angle $\hat{\alpha}$ is set to 30°, plane becomes parallel with the x-ray source. Therefore, information from this acquisition angle cannot contribute to reconstruction. In Figure 4.10, vertical line is observed due

to parallel position when angles were $\hat{\alpha}=30°$ and $\hat{\beta}=30°$, $50°$, $70°$.

$\hat{\beta}$	$\hat{\alpha}$	
	30°	50°
30°		
50°		
70°		
90°		
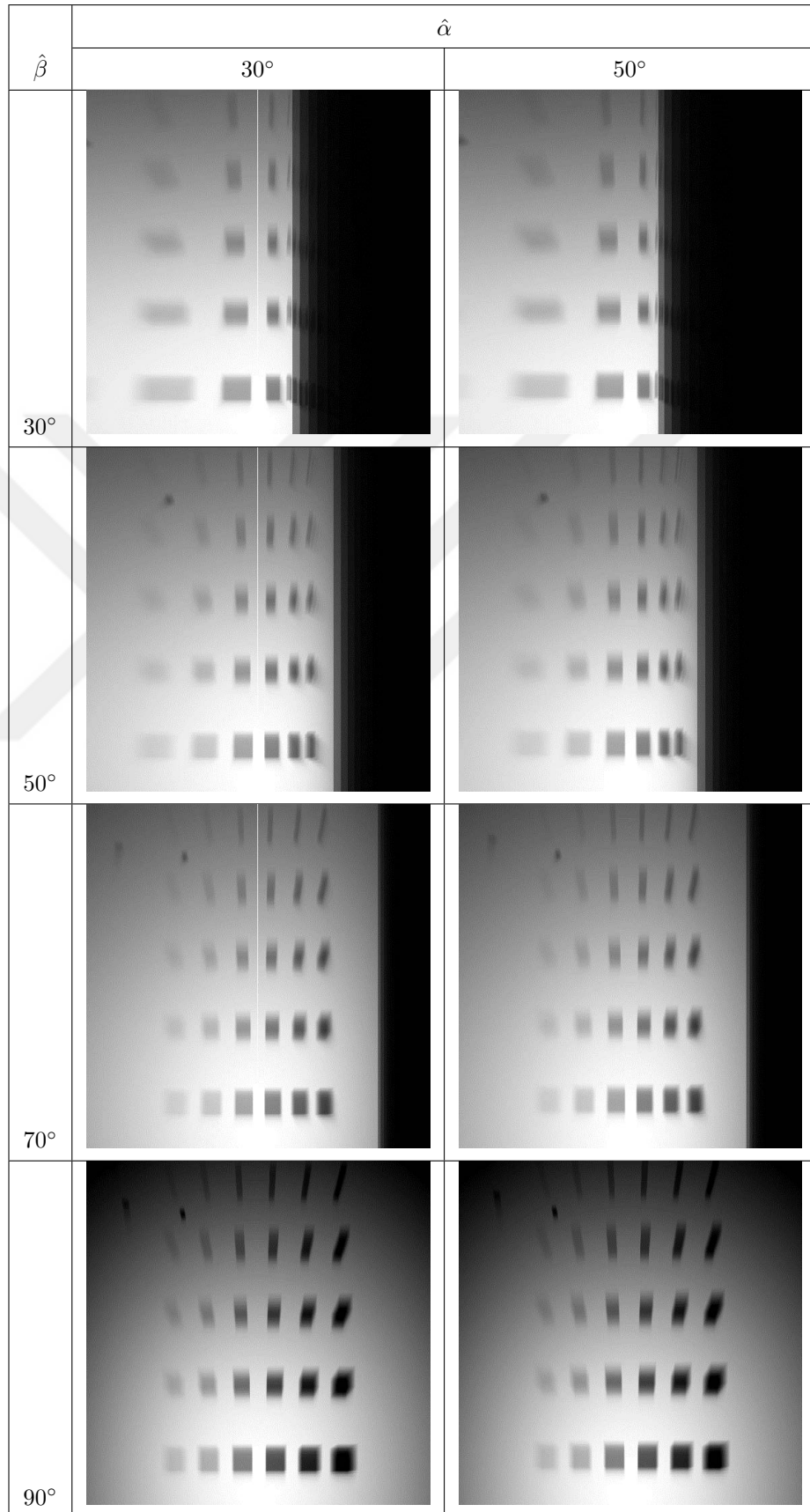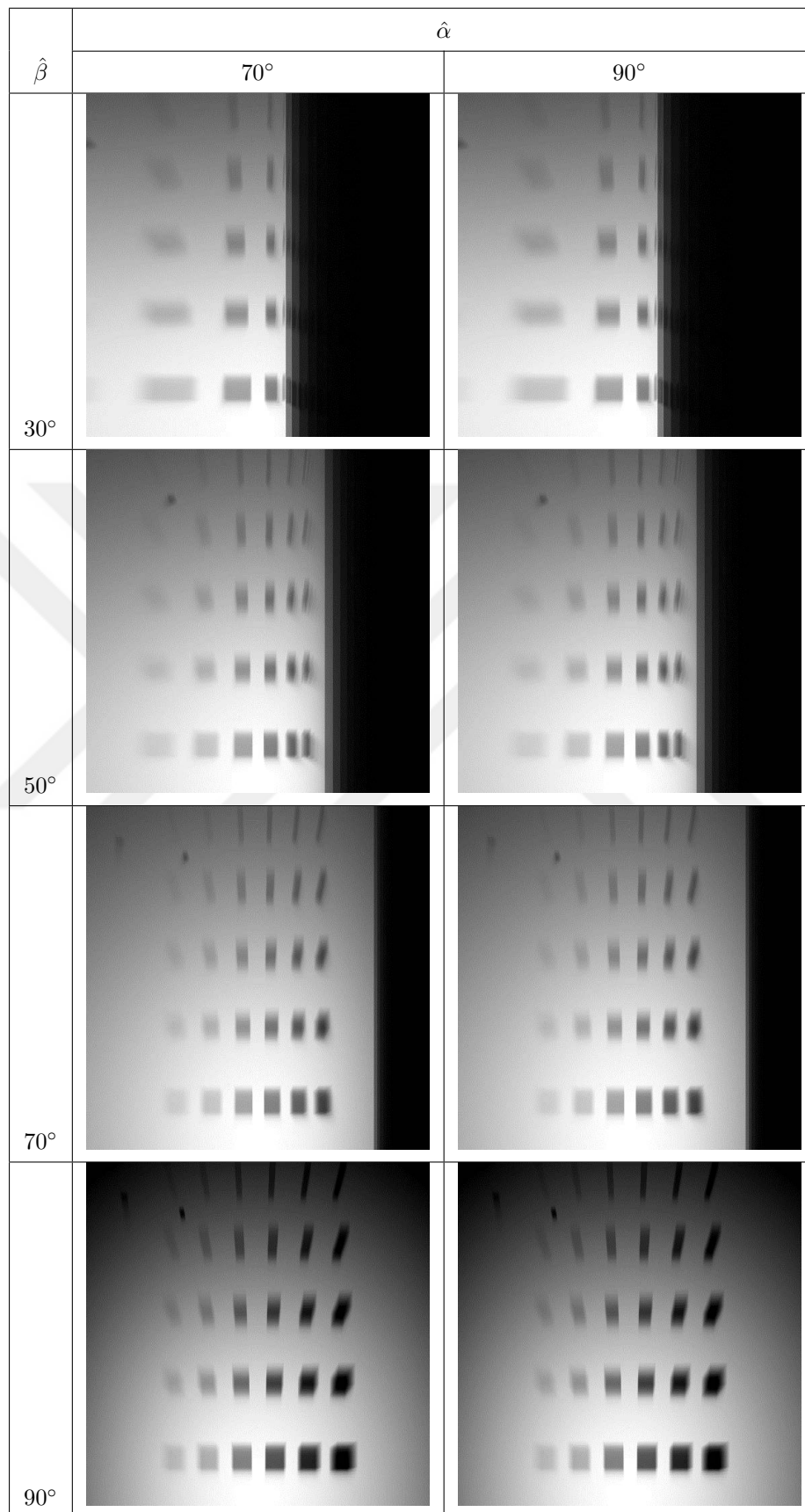
Figure 4.10 Simulated phantom reconstructed images at $l = 0$, $\hat{\beta} = 30°$, $50°$, $70°$, $90°$ and $\hat{\alpha} = 30°$, $50°$, $70°$, $90°$.
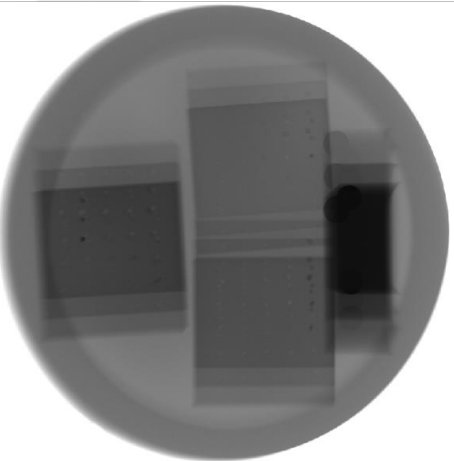
4.2.2 Tomosynthesis physical imaging results
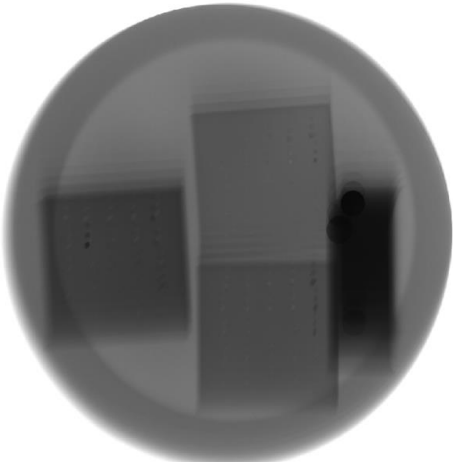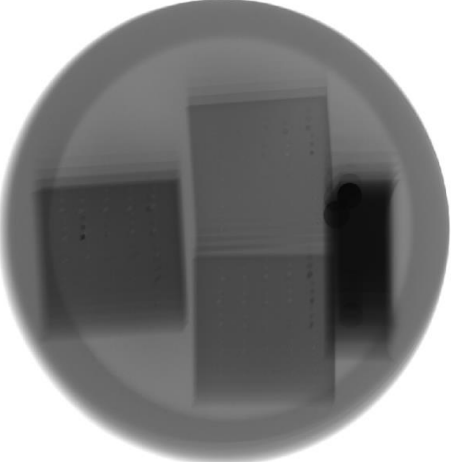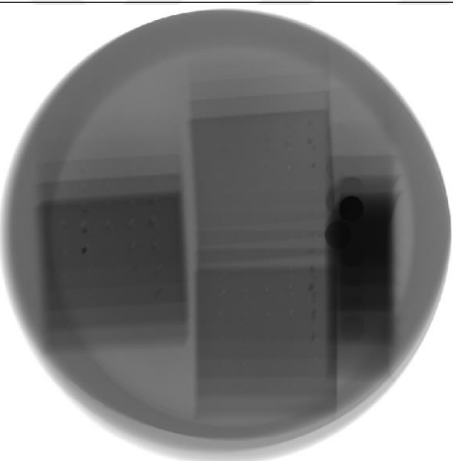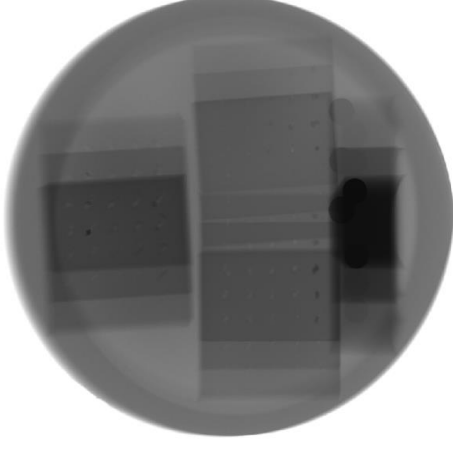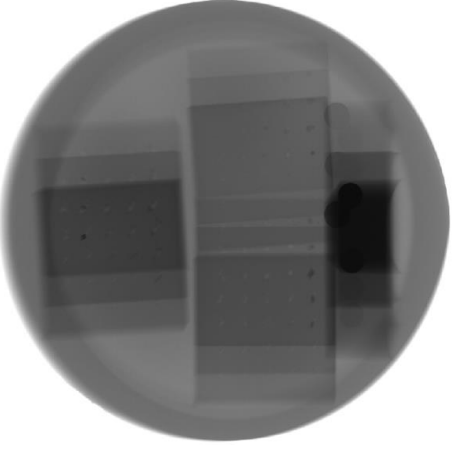
Similar to simulation, tomosynthesis images of physical phantom were created for 5 variables. Similar to simulation, MSSIM calculation for single projection reconstructions were not considered. Highest angle arc and lowest step size used as a reference image for comparisons. Table for selected variables is presented below.
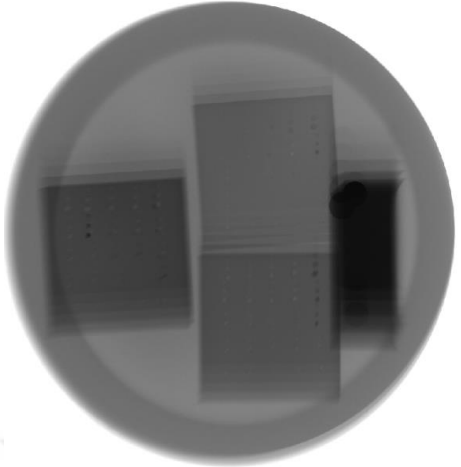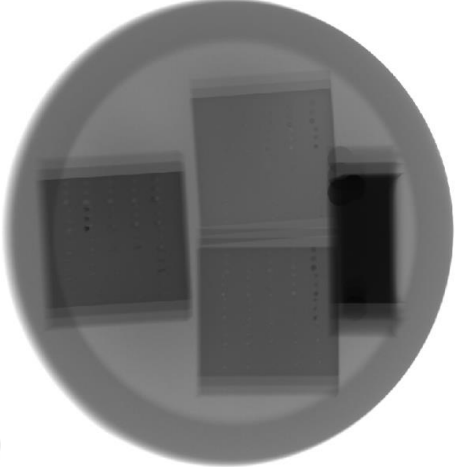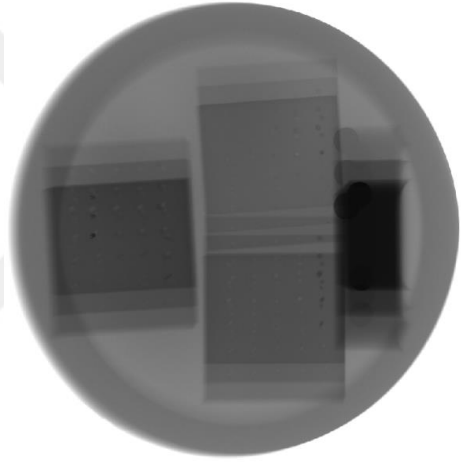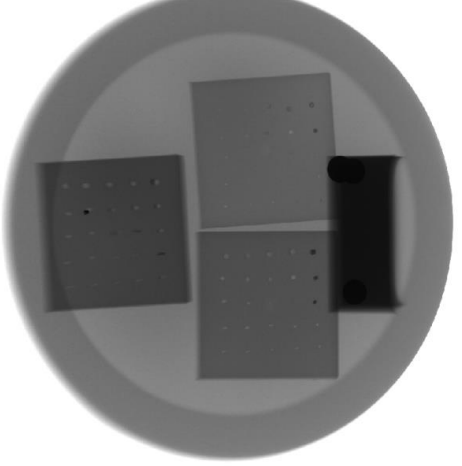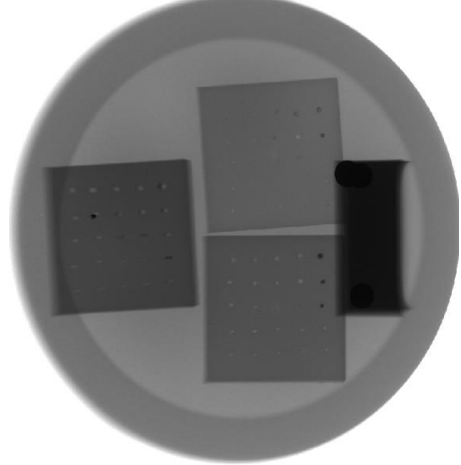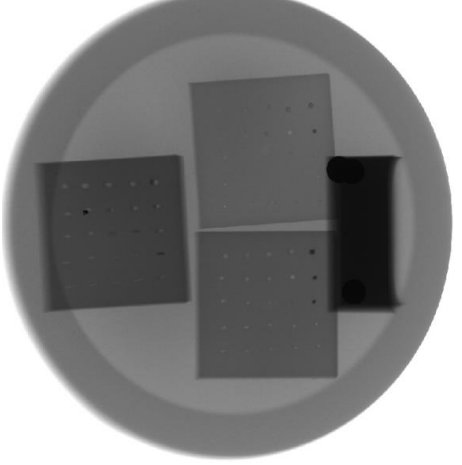
Table 4.5
Selected parameters for reconstruction of physical phantom images.

Acquisition arc	Step	Distance l	Angle $\hat{\alpha}$	Angle $\hat{\beta}$
24°, 18°,	9°, 6°,	−40 mm to 60 mm	90°, 70°,	90°, 70°,
12°, 6°	3°	with 10 mm steps	50°, 30°	50°, 30°

Firstly, phantom data was processed to create tomosynthesis image at distance $l = 10$ mm. Angle $\hat{\beta}$ and angle $\hat{\alpha}$ were equal to 90° for selected plane. Figure 4.11 presents the images for given properties.

Step	Range	
	24°	18°
3°		
6°		
9°		

	Range	
Step	12°	6°
3°		
6°		
9°		

Figure 4.11 Physical phantom reconstructed images at $l = 10$ mm, $\hat{\beta} = 90°$ and $\hat{\alpha} = 90°$.

Physical phantom images were taken with angle arc 24° with 3° steps. Planes are reconstructed with 24°, 18°, 12°, 6° angle arc and 9°, 6°, 3° steps. Reconstructed image with 24° arc and angle step 3° was used as a reference image. Selected plane was 10 mm above the isocenter and angles $\hat{\alpha}$, $\hat{\beta}$ were both 90° for first set of reconstructions. Figure 4.12 and Table 4.6 shows calculated MSSIM values for different angle arc and step sizes. Similarity index between images were decreased with closer angle arc. Note that 12° and 18° values with 6° step have same projection angles, so they are identical. Same situation also exists for 24° and 18° with 9° step. When 18° angle range with 6° and 9° steps are analyzed, role of angle range can be seen. In this case, ±6° and ±9° projections were used for steps 6° and 9° respectively. As it is seen, higher angle arc showed higher similarity with reference image.
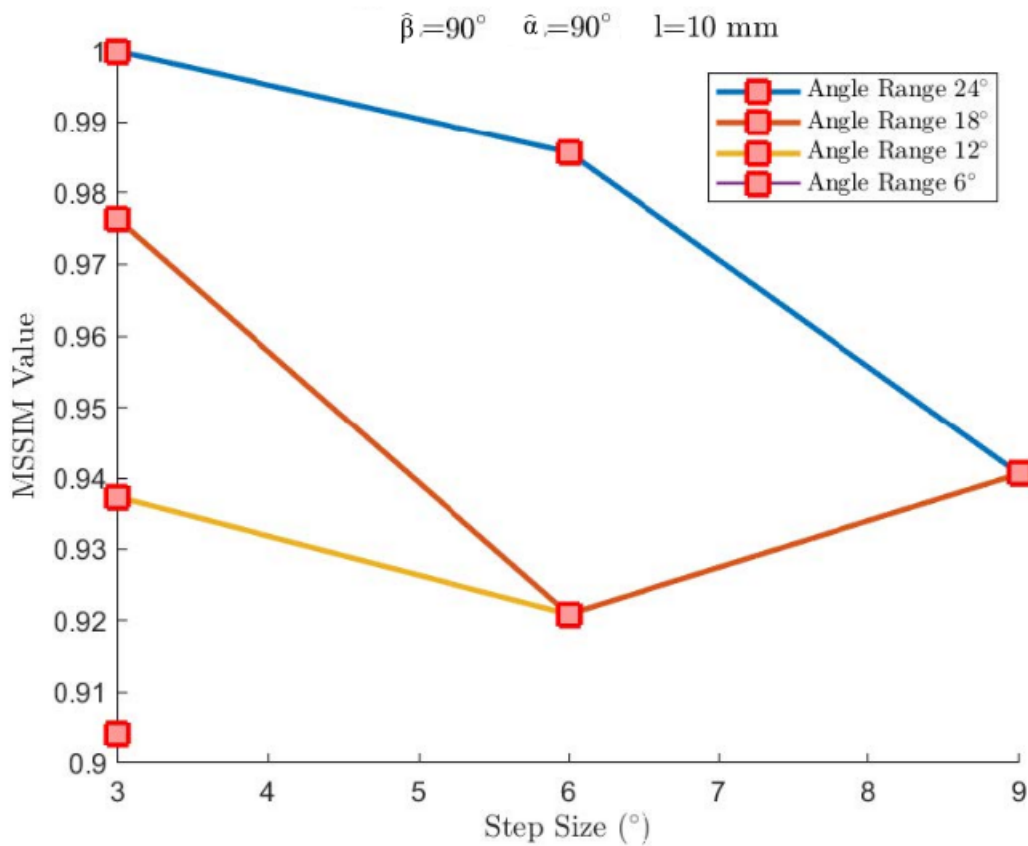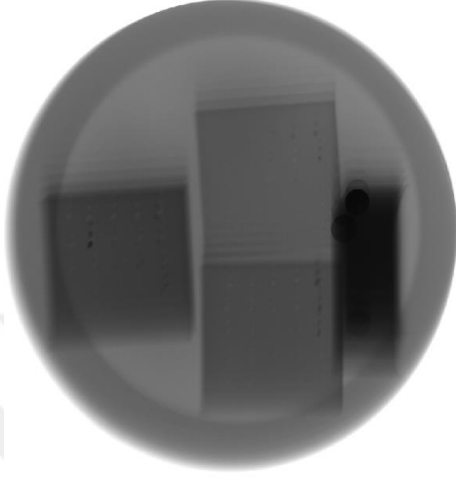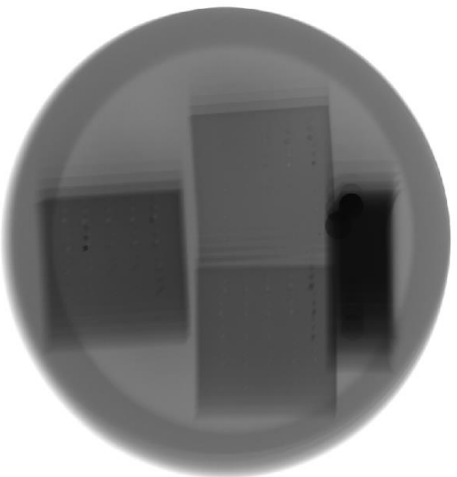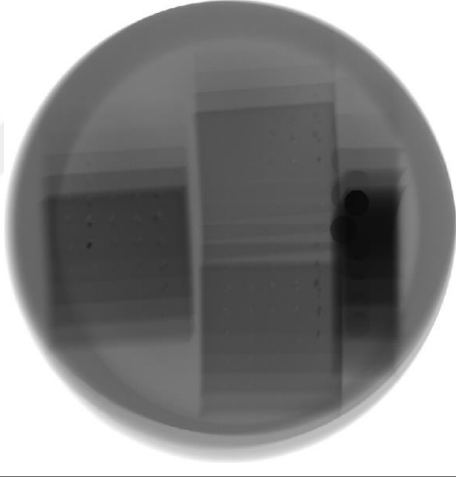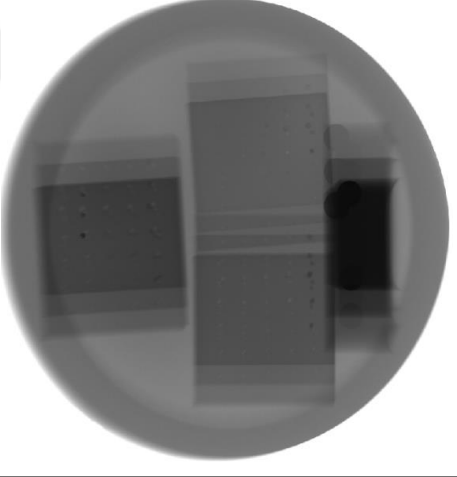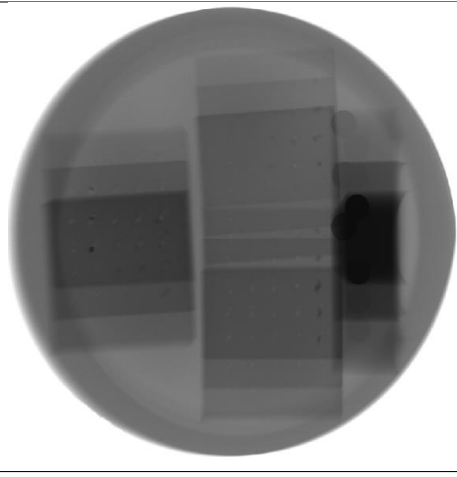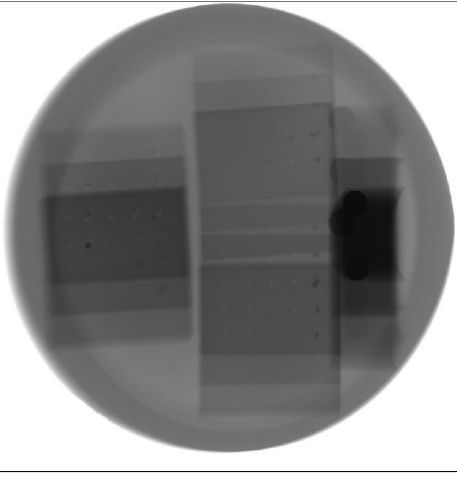

Figure 4.12 Mean structure similarity values (MSSIM) at $l = 10$ mm, $\hat{\beta} = 90°$ and $\hat{\alpha} = 90°$.

Table 4.6
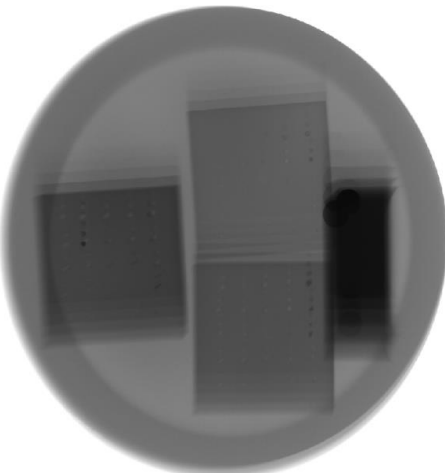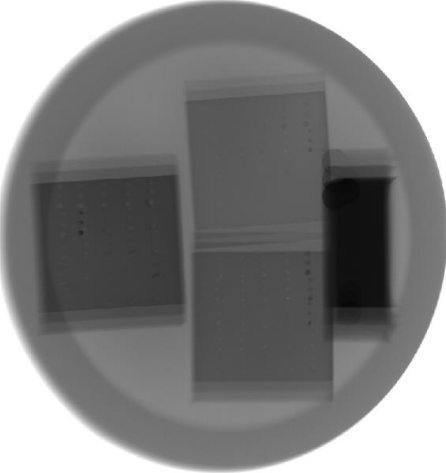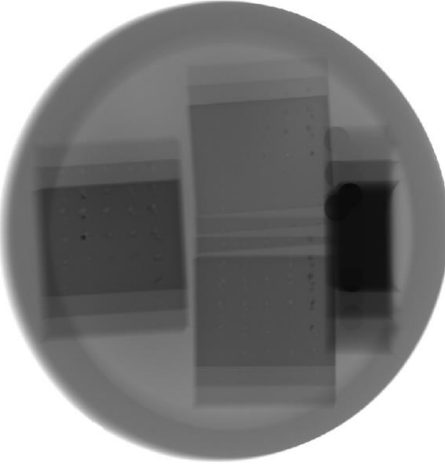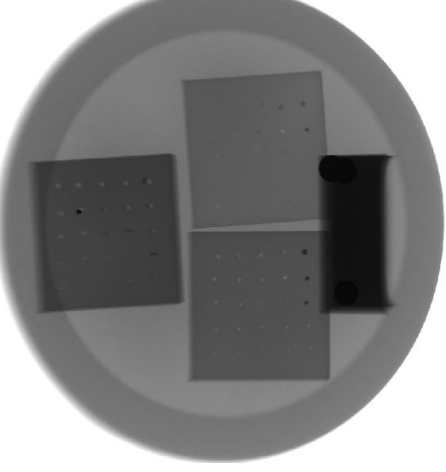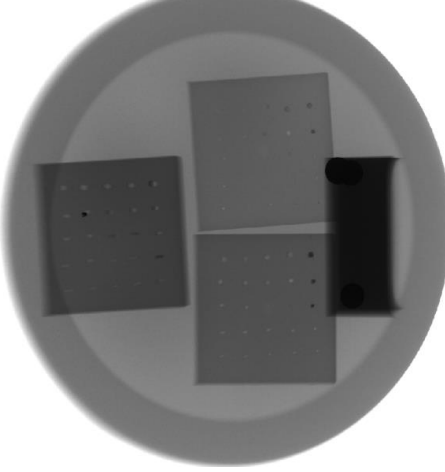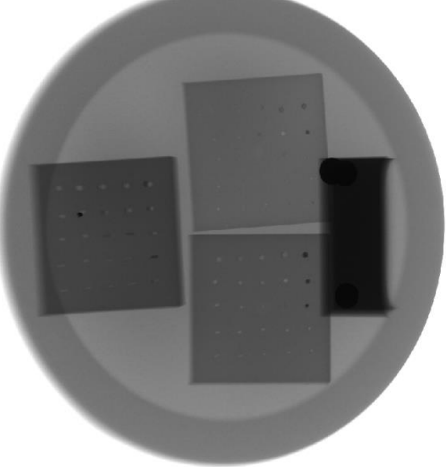Mean structure similarity values (MSSIM) $l = 10$ mm, $\hat{\beta} = 90°$ and $\hat{\alpha} = 90°$.

| Angle Range	Step	MSSIM	Number of Projections	Actual Angle Range
24	3	1	9	24
24	6	0.9857	5	24
24	9	0.9406	3	18
18	3	0.9763	7	18
18	6	0.9209	3	12
18	9	0.9406	3	18
12	3	0.9373	5	12
12	6	0.9209	3	12
6	3	0.9039	3	6

Next reconstruction was performed to analyze angle $\hat{\alpha}$ when it is reduced to 70°. Selected plane was at the isocenter and angle $\hat{\beta}$ was 90° (Figure 4.13).

Step	Range	
	24°	18°
3°		
6°		
9°		

	Range	
Step	12°	6°
3°		
6°		
9°		

Figure 4.13 Physical phantom reconstructed images at $l = 0$ mm, $\hat{\beta} = 90°$ and $\hat{\alpha} = 70°$.

Graphic comparison of MSSIM values are plotted in Figure 4.14. MSSIM values reduced with narrower acquisition arcs. For example, when number of projections was 3, reconstruction were performed at 18°, 12°, 6° arcs were showed decreasing trend in similarity with reference image.
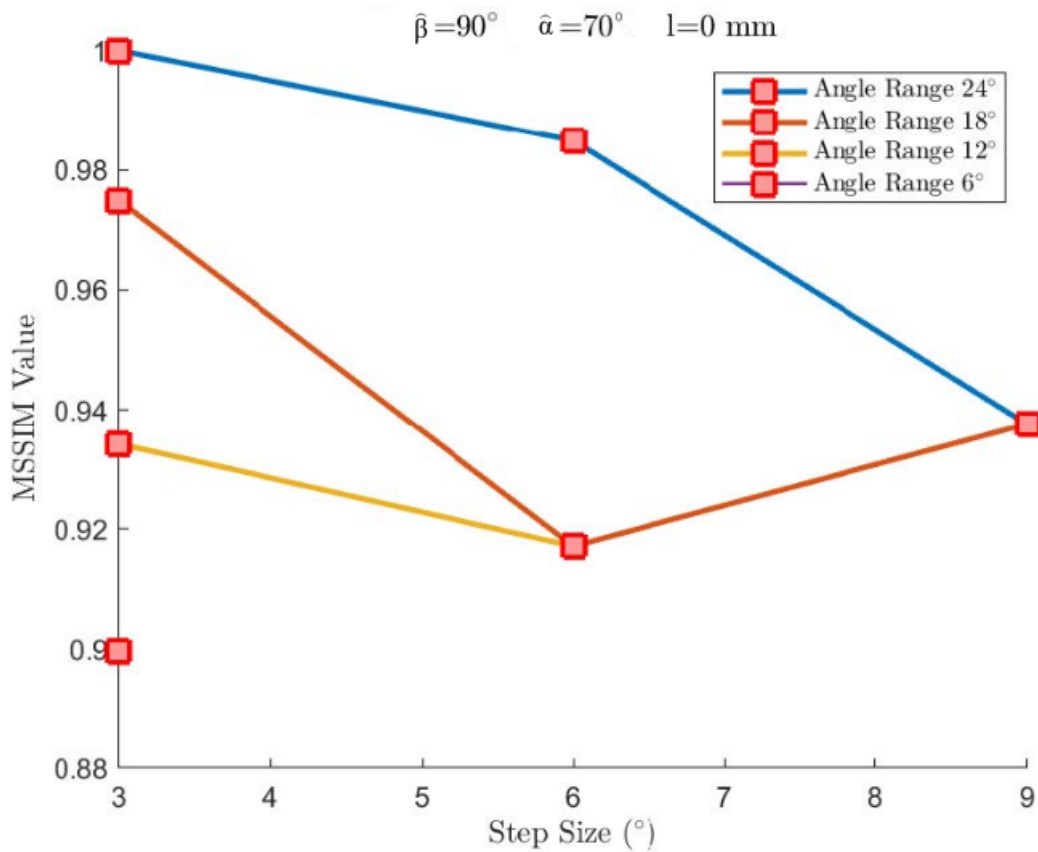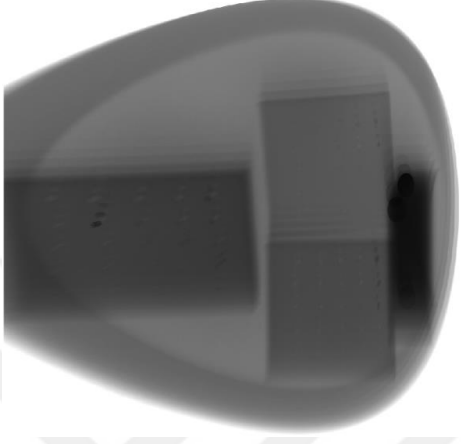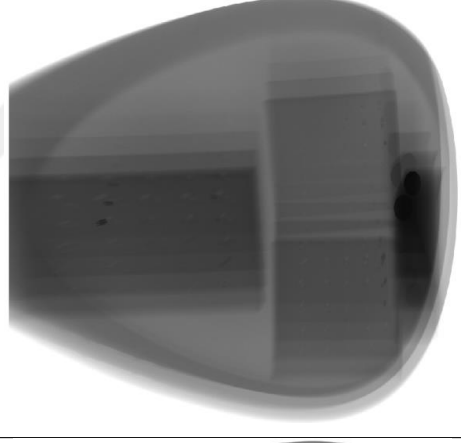

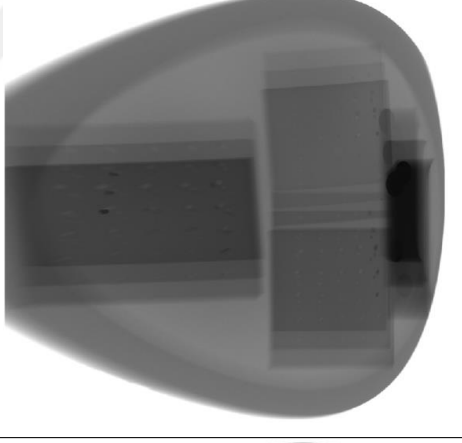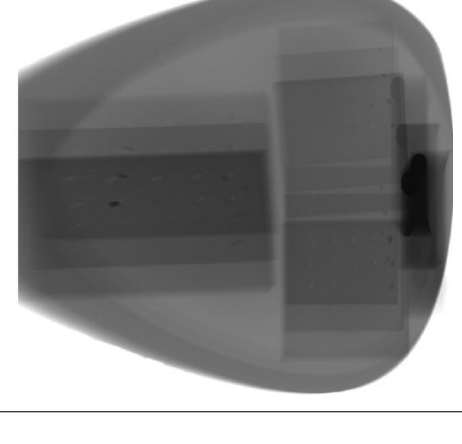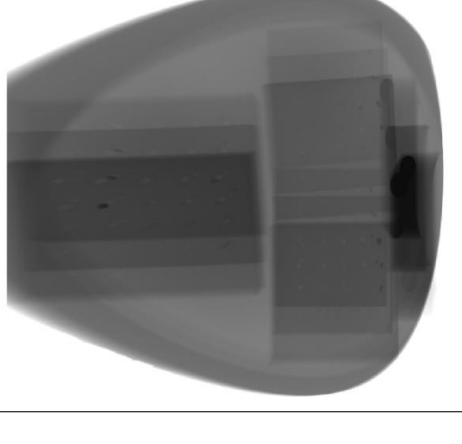**Figure 4.14** Mean structure similarity values (MSSIM) at $l = 0$ mm, $\hat{\beta} = 90°$ and $\hat{\alpha} = 70°$.
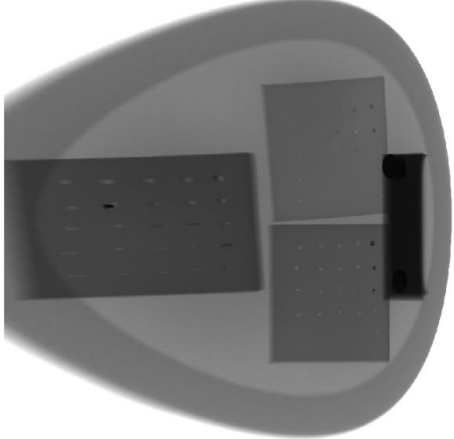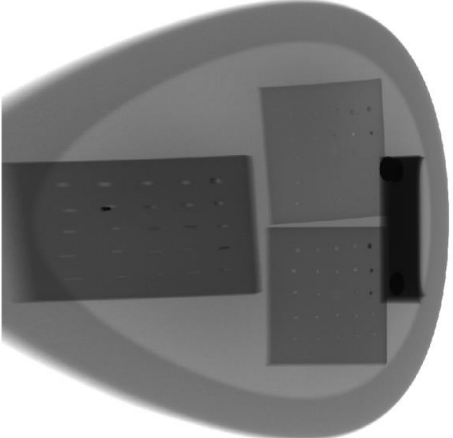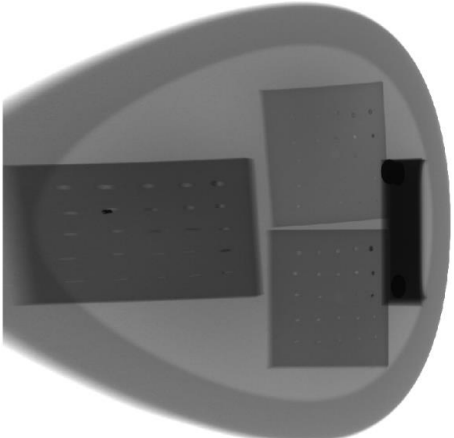
Table 4.7 demonstrates detailed information for Figure 4.14. When values in Table 4.6 and Table 4.7 were analyzed, it is seen that similarity between images were reduced more when angle $\hat{\alpha}$ is changed.

Table 4.7
Mean structure similarity values (MSSIM) $l = 0$ mm, $\hat{\beta} = 90°$ and $\hat{\alpha} = 70°$.

Angle Range	Step	MSSIM	Number of Projections	Actual Angle Range
24	3	1	9	24
24	6	0.9849	5	24
24	9	0.9375	3	18
18	3	0.9748	7	18
18	6	0.9171	3	12
18	9	0.9375	3	18
12	3	0.9342	5	12
12	6	0.9171	3	12
6	3	0.8996	3	6

Angle $\hat{\beta}$ was changed to 70° degrees for next reconstruction. Also, angle $\hat{\alpha}$ was set to 90° while distance l remained 0.

Step	Range	
	24°	18°
3°		
6°		
9°		

Step	Range	
	12°	6°
3°		
6°		
9°		

Figure 4.15 Physical phantom reconstructed images at $l = 0$ mm, $\hat{\beta} = 70°$ and $\hat{\alpha} = 90°$.

MSSIM values' relation with angle range and step angle are shown in Figure 4.16.

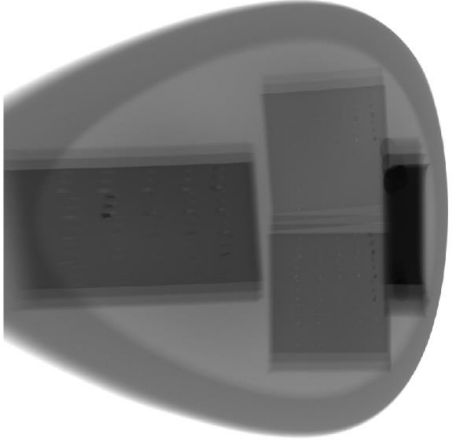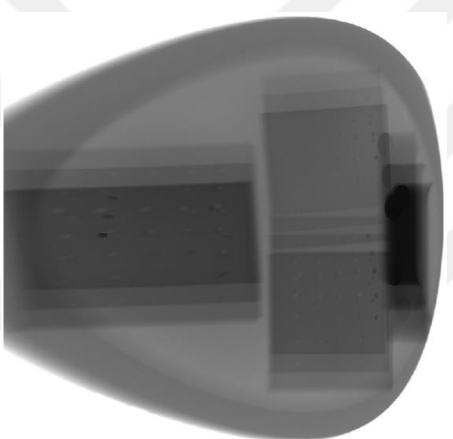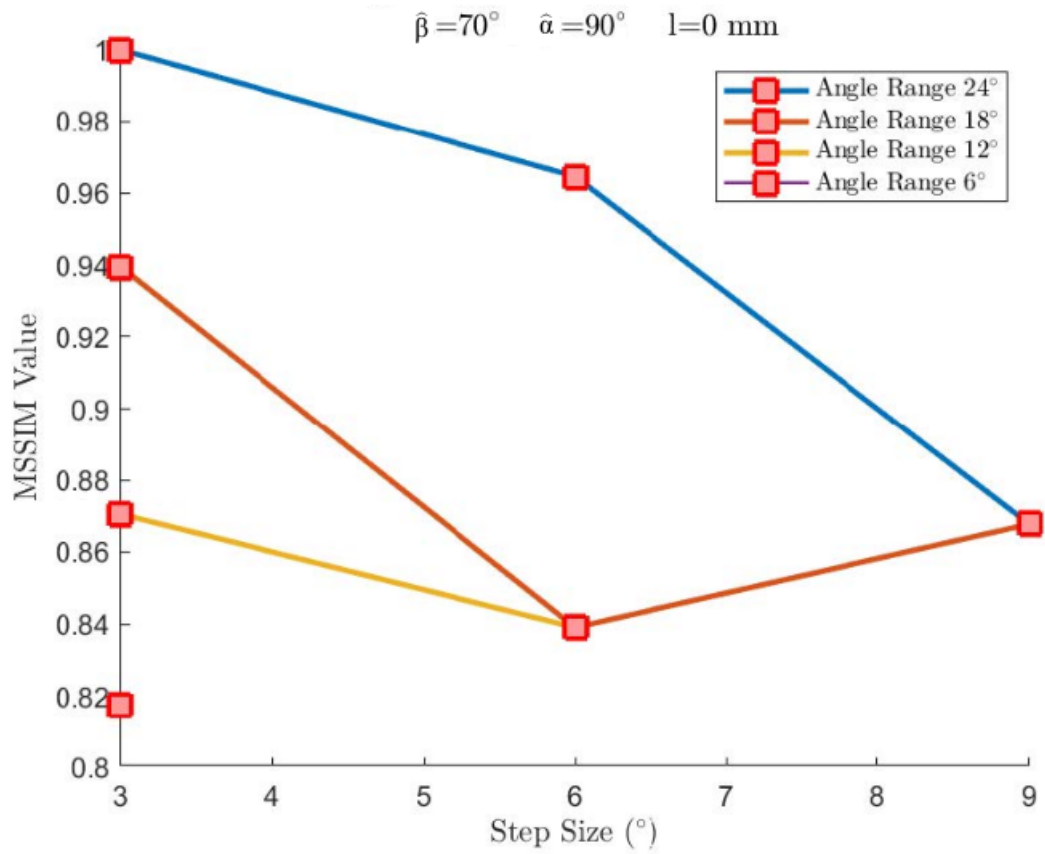**Figure 4.16** Mean structure similarity values (MSSIM) at $l = 0$ mm, $\hat{\beta} = 70°$ and $\hat{\alpha} = 90°$.

MSSIM values for the comparison are given in Table 4.8.
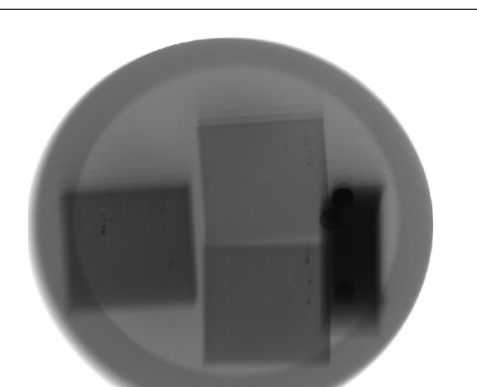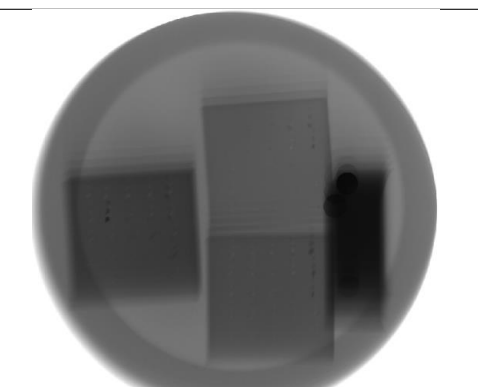
Table 4.8
Mean structure similarity values (MSSIM) $l = 0$ mm, $\hat{\beta} = 70°$ and $\hat{\alpha} = 90°$.

Angle Range	Step	MSSIM	Number of Projections	Actual Angle Range
24	3	1	9	24
24	6	0.9645	5	24
24	9	0.8677	3	18
18	3	0.9394	7	18
18	6	0.8390	3	12
18	9	0.8677	3	18
12	3	0.8705	5	12
12	6	0.8390	3	12
6	3	0.8175	3	6

As indicated earlier, x-ray tube's position changes in only x and z direction during acquisition. Therefore, reconstruction image was more distorted when angle between selected plane and y axis was changed. When Tables 4.6, 4.7 and 4.8 are compared, it can be seen that MSSIM values in Table 4.8 were lowest for same angle arcs and steps.

Similar to simulation section, object was reconstructed for various angle values. Images were created for 24° angle arc with 3° steps while selected plane was 20 mm above the isocenter plane. Acquired images can be seen in Figure 4.17 for different $\hat{\alpha}$ and $\hat{\beta}$ values. Similar to simulation, images were highly distorted when y axis tilted planes were selected. Especially, lower achievement in images at 30° and 50° were observed.

$\hat{\beta}$	$\hat{\alpha}$	
	30°	50°
30°		
50°		
70°		
90°		

$\hat{\beta}$	$\hat{\alpha}$	
	70°	90°
30°		
50°		
70°		
90°		
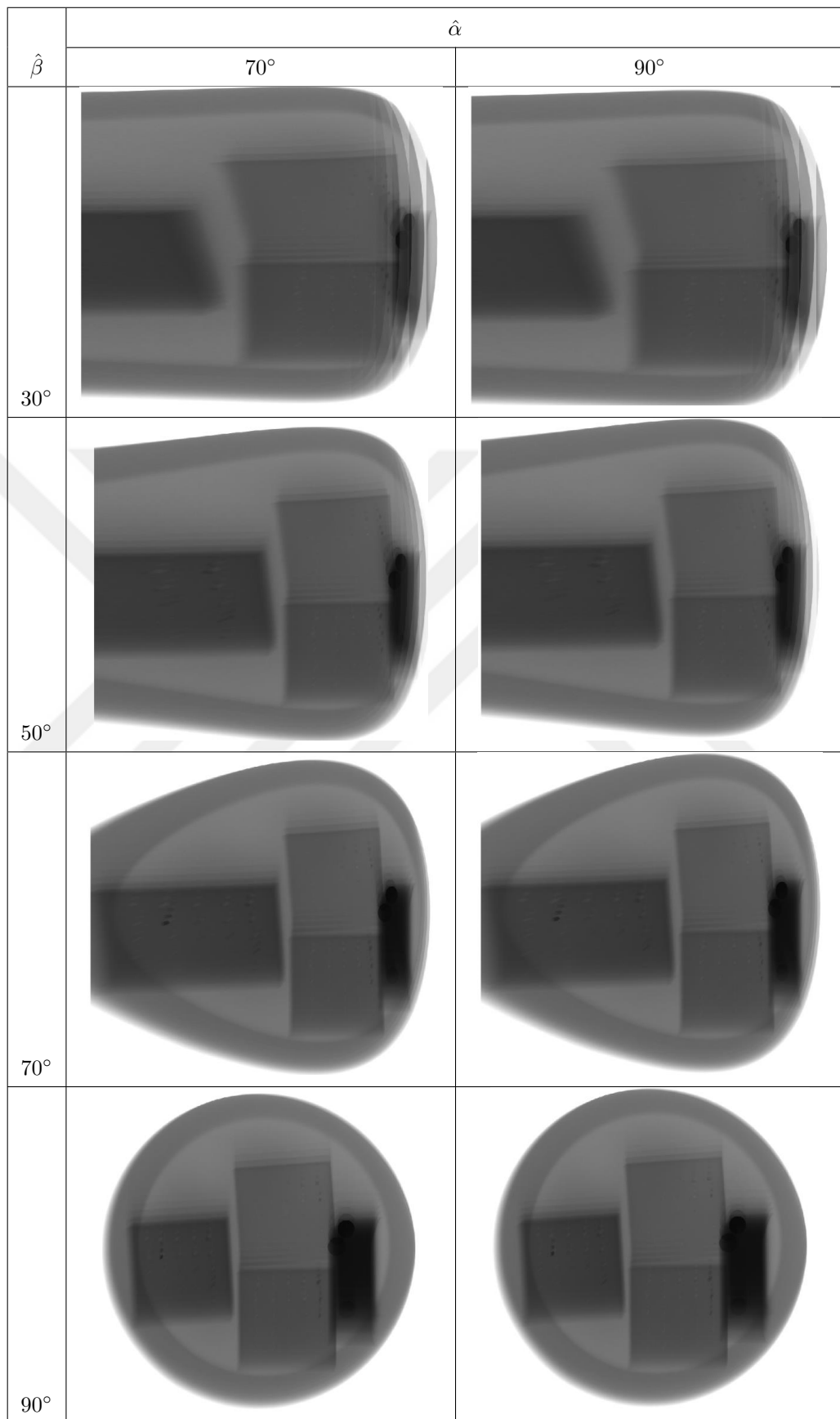
Figure 4.17 Physical phantom reconstructed images at $l = 20$ mm, $\hat{\beta} = 30°$, $50°$, $70°$, $90°$ and $\hat{\alpha} = 30°$, $50°$, $70°$, $90°$.

4.2.3 Removal of distortion inducing plane

Last analysis were performed for extraction of distortion inducing planes. Distortion removal applied on both images of simulation and physical phantom. Also, angle $\hat{\alpha}$ and $\hat{\beta}$ were 90° for each analysis. In simulated projection, distance l, angle range and steps size were -30, 60° and 2° respectively. Firstly, plane at -50 is removed from reconstruction image then planes between -50 to -60 were extracted. Figure 4.18 shows these images.

Selected plane image	Image after plane at l=−50 is removed.
Image after planes at l=−50 to −60 are removed.	
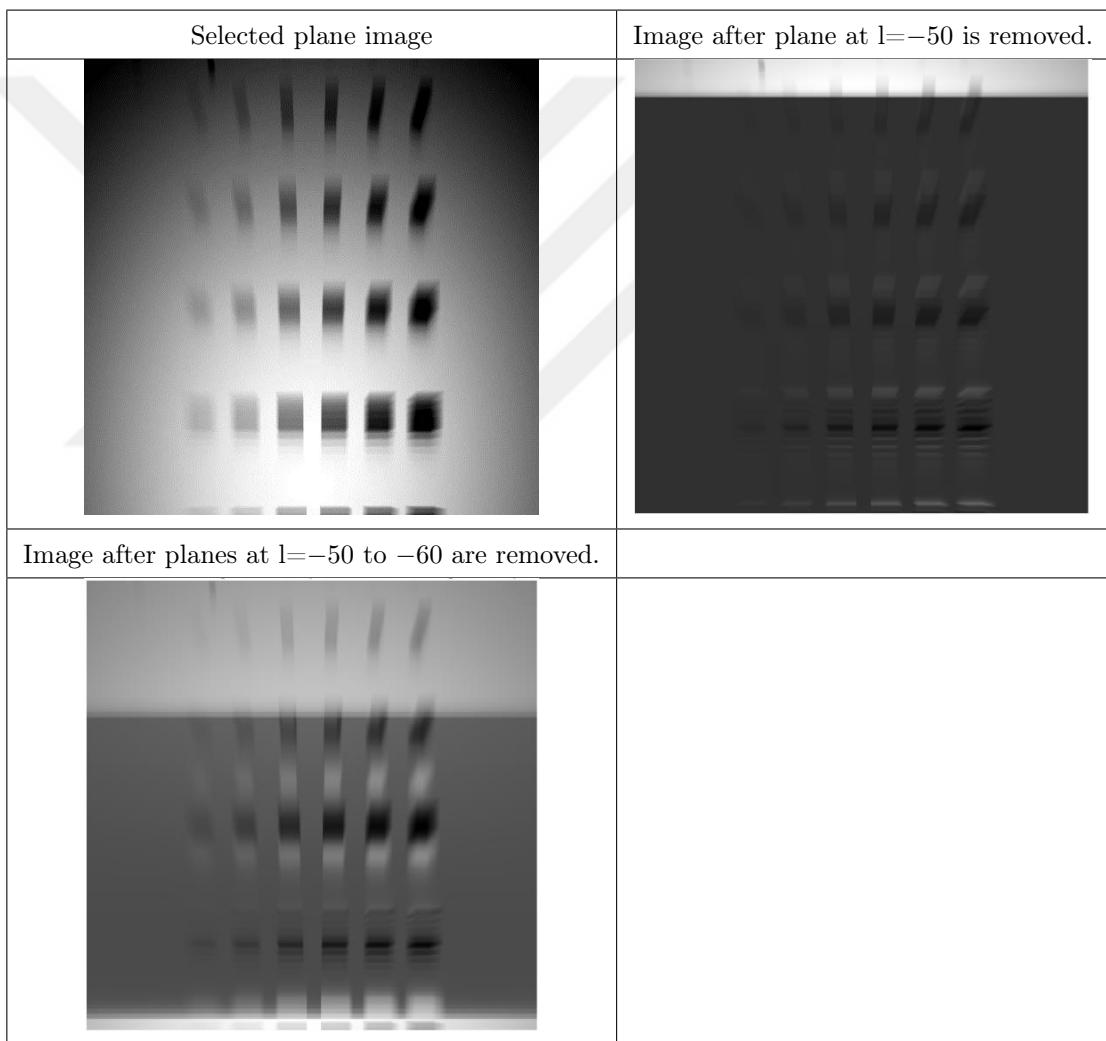
Figure 4.18 Simulated phantom reconstructed images at $l = -30$, $\hat{\beta} = 90°$ and $\hat{\alpha} = 90°$.

Histograms are plotted for these images are demonstrated in Figure 4.19. When the histograms of the images presented in Figure 4.19 were analyzed, it was seen that higher values were removed from the images.
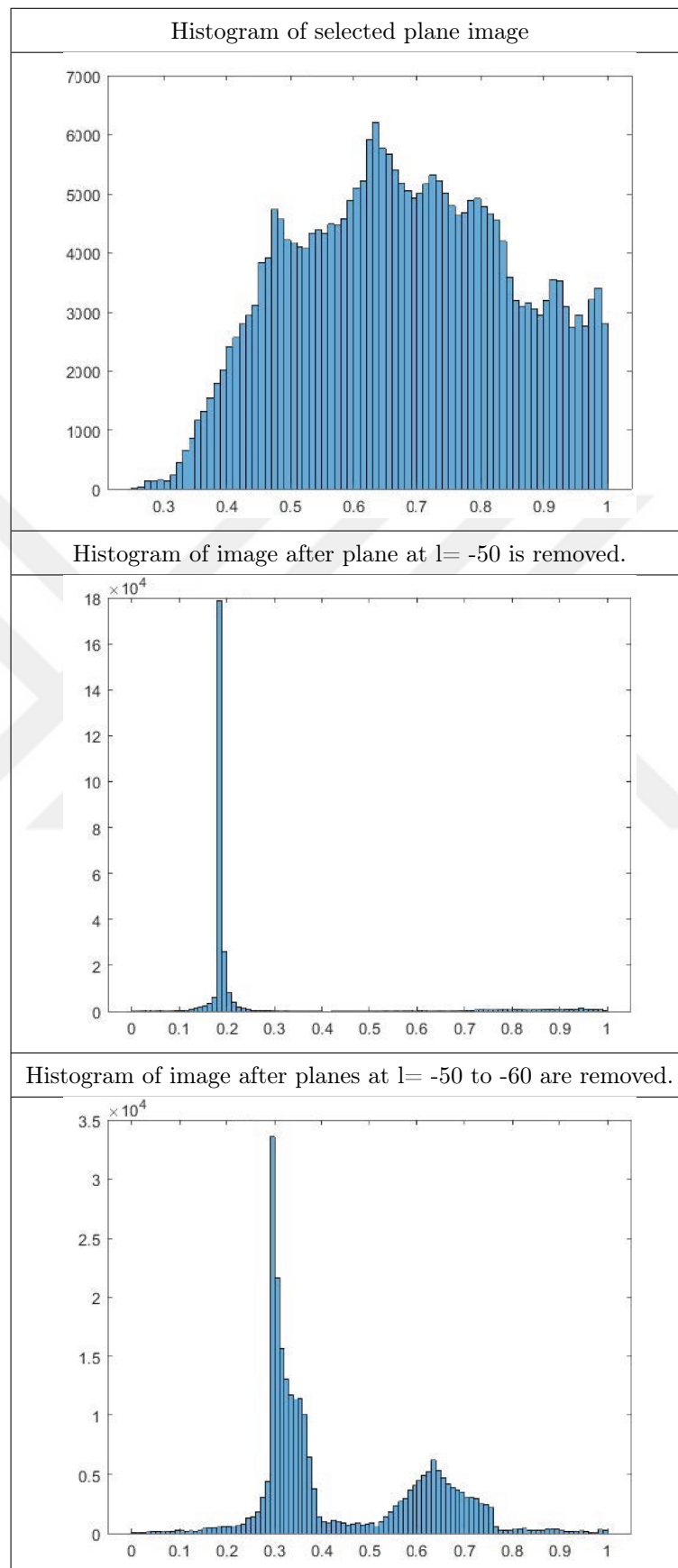
Figure 4.19 Histograms for simulated phantom reconstructed images at $l = -30$, $\hat{\beta} = 90°$ and $\hat{\alpha} = 90°$.

Similar to simulation, removal of out of plane structures were performed for physical phantom. Selected plane was 10 mm distant from the isocenter while distortion inducing plane was at isocenter. Images were constructed from projections at 24° arc and 3° steps. In the first case, subtracted plane was placed at isocenter. In the second case, planes both above and below the selected plane were used for removal process. Planes at −40, −30, −20, −10, 0, 20, 30, 40 mm were removed. Reconstruction images were shown in Figure 4.20. It can be seen that visibility of the holes increased after distortion removal. Similar to simulation, histograms in Figure 4.21 shows that high intensity values are extracted from the image after plane removal.

Selected plane image	Image after plane at l=0 mm is removed.
Image after planes at l= −40, −30, −20, −10, 0, 20, 30, 40 mm are removed.	
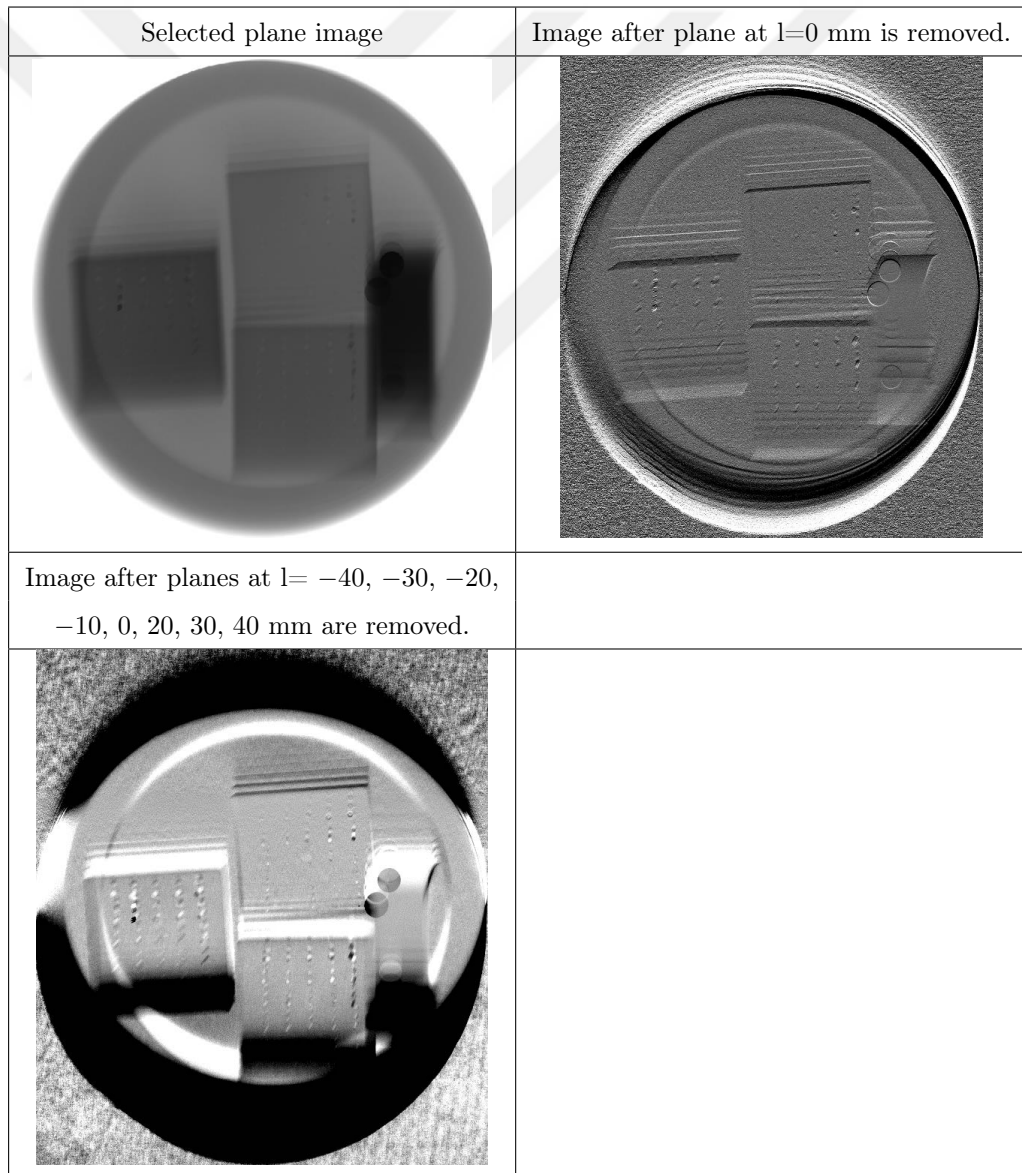
Figure 4.20 Physical phantom reconstructed images at $l = 10$ mm, $\hat{\beta} = 90°$ and $\hat{\alpha} = 90°$.
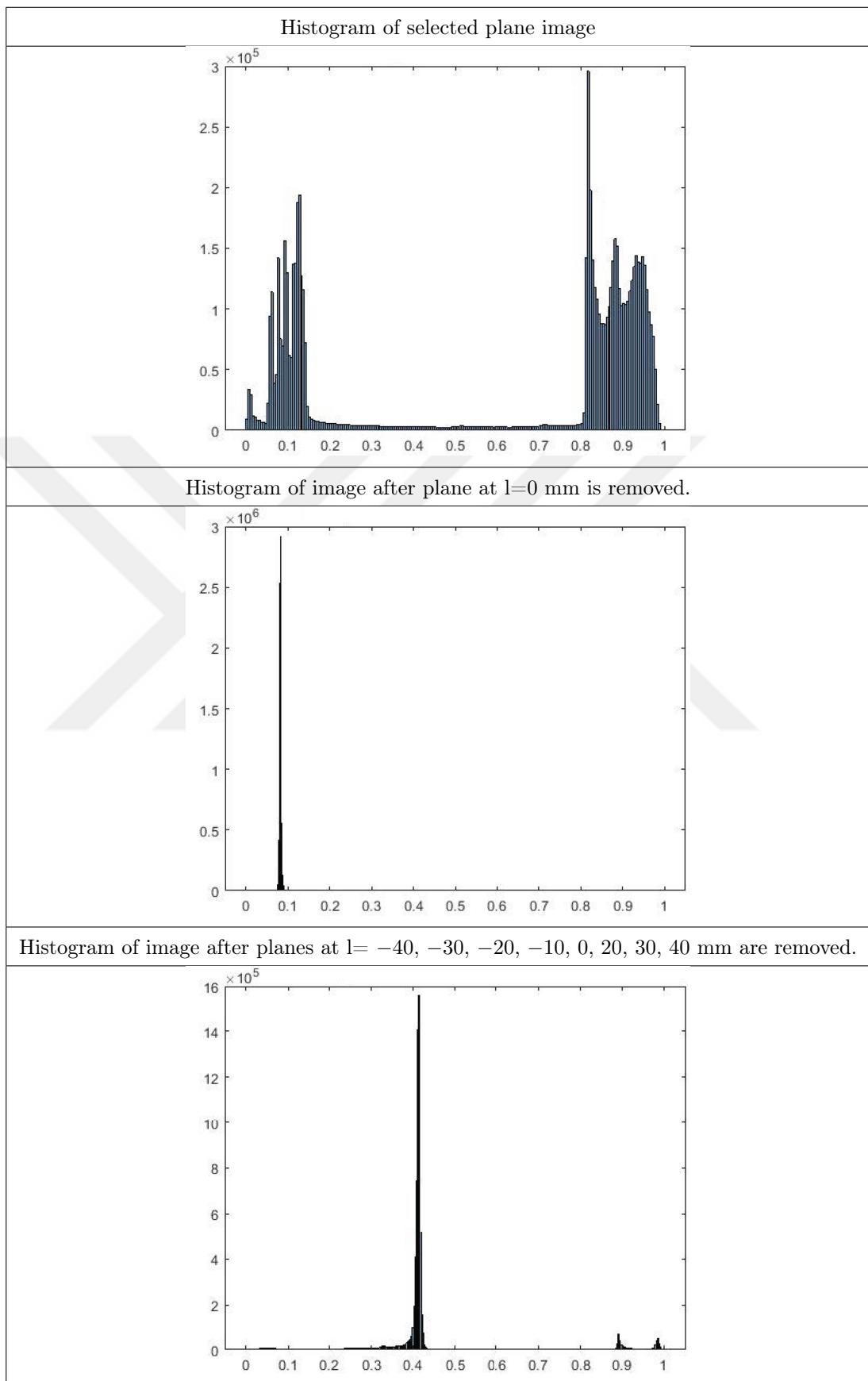
Figure 4.21 Histogram for physical phantom reconstructed images at $l = 10$ mm, $\hat{\beta} = 90°$ and $\hat{\alpha} = 90°$.

5. CONCLUSION

Tomosynthesis using a stationary detector system is examined for this thesis. Effect of variables $(\hat{\beta}, \hat{\alpha}, l)$ are observed with both simulation and physical phantom data. It was seen that acquisition angle is important factor for image reconstruction. In most cases, higher similarities were achieved with wider range. Also, it was shown that y axis tilted image reconstructions are limited due to x-ray tube's movement. Distortion removal helped to better identification of structures. Small holes in the phantom were able to be seen clearer after planes were subtracted.

Image reconstruction algorithm is able to create images from different planes with decent quality to improve the identification of the structures in those plane. Since it uses less projections for image construction, it can help to reduce patient's radiation exposure.

Energy, current, and exposure time were same for physical phantom images. Unfortunately greater angle could not be tested due to capabilities of the current system. As a future work; image reconstruction for different x-ray tube's specifications may be investigated. Also, simulation algorithm may include focal spot size, detector noise and stochastic model. Additionally, feasibility of a system that moves in both x and y axis may also be explored.

REFERENCES

1. Z. Kolitsi, G. Panayiotakis, V. Anastassopoulos, A. Scodras, and N. Pallikarakis, "A multiple projection method for digital tomosynthesis," *Med Phys*, vol. 19, no. 4, pp. 1045–50, 1992. (Accessed Feb. 10, 2015).

2. J. T. Dobbins and D. J. Godfrey, "Digital x-ray tomosynthesis: current state of the art and clinical potential," *Physics in Medicine and Biology*, vol. 48, no. 19, pp. R65–R106, 2003.

3. "Wilhelm conrad röntgen - biographical." [Online]. Available: http://www.nobelprize.org/nobel_prizes/physics/laureates/1901/rontgen-bio.html. (Accessed Aug. 24, 2016).

4. P. Suetens, *Fundamentals of Medical Imaging.* Cambridge University Press, 2002.

5. A. Dhawan, *Medical Image Analysis.* Wiley, 2003.

6. C. R. Nave, "X-rays." [Online]. Available: http://hyperphysics.phy-astr.gsu.edu/hbase/quantum/xrayc.html. (Accessed Sept. 23, 2016).

7. G. Zschornack, *Handbook of X-Ray Data.* Springer Berlin Heidelberg, 2007.

8. J. A. Seibert and J. M. Boone, "X-ray imaging physics for nuclear medicine technologists. part 2: X-ray interactions and image formation," *J Nucl Med Technol*, vol. 33, no. 1, pp. 3–18, 2005. (Accessed Feb. 15, 2015).

9. J. Kelly, "X-rays for diagnosis." [Online]. Available: http://img.chem.ucl.ac.uk/www/kelly/medicalxrays.htm. (Accessed Feb. 15, 2015).

10. J. H. Wittke, "Signals," 2016. [Online]. Available: https://www2.nau.edu/microanalysis/wordpress/index.php/signals/. (Accessed Aug. 9, 2019).

11. J. Bushberg, *The Essential Physics of Medical Imaging.* Lippincott Williams & Wilkins, 2002.

12. J. T. Dobbins, "Tomosynthesis imaging: At a translational crossroads," *Medical Physics*, vol. 36, no. 6, p. 1956, 2009.

13. P. Dawkins, "Classes-calculus iii-equations of lines," 2018. [Online]. Available: http://tutorial.math.lamar.edu/Classes/CalcIII/EqnsOfLines.aspx. (Accessed July 13, 2019).

14. P. Duvauchelle, N. Freud, V. Kaftandjian, and D. Babot, "A computer code to simulate x-ray imaging techniques," *Nuclear Instruments and Methods in Physics Research Section B: Beam Interactions with Materials and Atoms*, vol. 170, no. 1-2, pp. 245–258, 2000.

15. W. P. Argo, K. Hintenlang, and D. E. Hintenlang, "A tissue-equivalent phantom series for mammography dosimetry," *J Appl Clin Med Phys*, vol. 5, no. 4, pp. 112–9, 2004. [Online]. Available: https://www.ncbi.nlm.nih.gov/pubmed/15738925. (Accessed July 15, 2019).

16. T. Gomi, "State-of-the-art x-ray digital tomosynthesis imaging," in *Medical Imaging and Image-Guided Interventions*, R. A. Sebro, Ed. Rijeka: IntechOpen, 2018, ch. 5. [Online]. Available: https://doi.org/10.5772/intechopen.81667

17. T. Kellner, "Engineered by women for women: Colleagues band together to take fear out of breast screening," Nov. 26, 2017 2017. [Online]. Available: https://www.ge.com/reports/engineered-women-women-colleagues-band-together-take-fear-breast-screening/. (Accessed July 15, 2019).

18. D. Soimu, Z. Kolitsi, and N. Pallikarakis, "A reconstruction algorithm with selective removal of out of plane structures for digital tomosynthesis using a stationary detector," in *Connecting Medical Informatics and Bio-Informatics, R. Engelbrecht et al. (Eds.), ENMI*, 2005, Journal Article, pp. 1192–1197.

19. Z. Kolitsi, G. Panayiotakis, and N. Pallikarakis, "A method for selective removal of out-of-plane structures in digital tomosynthesis," *Med Phys*, vol. 20, no. 1, pp. 47–50, 1993. (Accessed Feb. 10, 2015).

20. A. Varılsüha, "Implementation of tomosynthesis in dental x-ray imaging," M.S. thesis, Inst. of Biomed. Eng., Boğaziçi Univ., İstanbul, Turkey, 2012.

21. Z. Wang, A. C. Bovik, H. R. Sheikh, and E. P. Simoncelli, "Image quality assessment: From error visibility to structural similarity," *IEEE Transactions on Image Processing*, vol. 13, no. 4, pp. 600–612, 2004.

22. Z. Wang, "Ssim index with automatic downsampling," 2009. [Online]. Available: https://www.cns.nyu.edu/~lcv/ssim/ssim.m

23. "Senographe pristina™, senographe pristina™ 3d, senobright™ hd, system versions nga 1.20 and ngb 2.2.50, dicom conformance statement." [Online]. Available: http://www3.gehealthcare.com/~/media/documents/us-global/products/interoperability/dicom/xray/gehc-dicom-conformance_senographe-pristina-3d-nga-1-20-ngb-2-2-50_5721674-1-8en_rev2.pdf. (Accessed Aug. 5, 2019).